Pacific
Northwest
NATIONAL LABORATORY

PNNL-39196

DEMO-FTES: Development, Monitoring, and Control of Fracture Thermal Energy Storage in Crystalline Rock Formations (CRADA 580) Final Report

February 2026

Jeffrey Burghardt
Brice Lecampion
Yingqi Zhang
Mathew Ingraham
Leon Hibbard
Ambroise Mathey
Andreas Möri
Dana Sirota
Dorothy Linneman

U.S. DEPARTMENT OF ENERGY

Prepared for the U.S. Department of Energy
under Contract DE-AC05-76RL01830

NOTICE

This report was produced by Battelle Memorial Institute under Contract No. DE-AC05-76RL01830 with the Department of Energy. During the period of commercialization or such other time period specified by the Department of Energy, the Government is granted for itself and others acting on its behalf a nonexclusive, paid-up, irrevocable worldwide license in this data to reproduce, prepare derivative works, and perform publicly and display publicly, by or on behalf of the Government. Subsequent to that period, the Government is granted for itself and others acting on its behalf a nonexclusive, paid-up, irrevocable worldwide license in this data to reproduce, prepare derivative works, distribute copies to the public, perform publicly and display publicly, and to permit others to do so. The specific term of the license can be identified by inquiry made to the Contractor or DOE. NEITHER THE UNITED STATES NOR THE UNITED STATES DEPARTMENT OF ENERGY, NOR ANY OF THEIR EMPLOYEES, MAKES ANY WARRANTY, EXPRESS OR IMPLIED, OR ASSUMES ANY LEGAL LIABILITY OR RESPONSIBILITY FOR THE ACCURACY, COMPLETENESS, OR USEFULNESS OF ANY DATA, APPARATUS, PRODUCT, OR PROCESS DISCLOSED, OR REPRESENTS THAT ITS USE WOULD NOT INFRINGE PRIVATELY OWNED RIGHTS.

Printed in the United States of America

Available to DOE and DOE contractors from the Office of Scientific and Technical
Information, P.O. Box 62, Oak Ridge, TN 37831-0062
www.osti.gov
ph: (865) 576-8401
fox: (865) 576-5728
email: reports@osti.gov

Available to the public from the National Technical Information Service
5301 Shawnee Rd., Alexandria, VA 22312 ph: (800) 553-NTIS (6847)
or (703) 605-6000
email: info@ntis.gov
Online ordering: http://www.ntis.gov

PNNL-39196

DEMO-FTES: Development, Monitoring, and Control of Fracture Thermal Energy Storage in Crystalline Rock Formations (CRADA 580) Final Report

February 2026

Jeffrey Burghardt
Brice Lecampion
Yingqi Zhang
Mathew Ingraham
Leon Hibbard
Ambroise Mathey
Andreas Möri
Dana Sirota
Dorothy Linneman

Prepared for the U.S. Department of Energy under Contract DE-AC05-76RL01830

Pacific Northwest National Laboratory
Richland, Washington 99354

PNNL-39196

Cooperative Research and Development Agreement (CRADA) Final Report

Report Date:

In accordance with Requirements set forth in the terms of the CRADA, this document is the CRADA Final Report, including a list of Subject Inventions, to be provided to PNNL Information Release who will forward to the DOE Office of Scientific and Technical Information as part of the commitment to the public to demonstrate results of federally funded research. **PNNL acknowledges that the CRADA parties have been involved in the preparation of the report or reviewed the report.**

Parties to the Agreement:

Batelle Memorial Institute

Lawrence Berkeley National Laboratory

National Technology Engineering Solutions of Sandia LLC

Swiss Federal Institute of Technology-Lausanne

CRADA number: 580

CRADA Title: DEMO-FTES: Development, Monitoring, and Control of Fracture Thermal Energy Storage in Crystalline Rock Formations

Responsible Technical Contact at DOE Lab(PNNL): Jeffrey Burghardt

Name and Email Address of POC at Partner Company(ies):

Lawrence Berkeley National Laboratory: Yingqi Zhang (yqzhang@lbl.gov)

National Technology Engineering Solutions of Sandia LLC: Mathew Ingraham (mdingr@sandia.gov)

Swiss Federal Institute of Technology-Lausanne: Brice Lecampion (brice.lecampion@epfl.ch)

Sponsoring DOE Program Office(s): Office of Geothermal

Joint Work Statement Funding Table showing DOE funding commitment:

	Funding Amounts			
CRADA Parties	**DOE Funding**		***In-kind**	

		Funds-In		Total
Participant(s)	NTESS: $200,000 LBNL: $150,000		EPFL:$255,281	
DOE Funding to PNNL	$650,000	N/A	N/A	
Total of all Contributions	$1,255,281			

Provide a list of publications, conference papers, or other public releases of results, developed under this CRADA:

Abstracts

1. Burghardt J.A., D. Sirota, B. Lecampion, D.C. Linneman, Y. Zhang, and L.E. Hibbard. 12/09/2024. "Design and Operation of a Meso-Scale Fracture Thermal Energy Storage Test." Abstract submitted to AGU 2024, Washington, District Of Columbia. PNNL-SA-202027.
2. A Mathey, A Möri, J Burghardt, B Lecampion, “Laboratory Scale Investigation of Fracture Thermal Energy Storage”, Sixth EAGE Global Energy Transition Conference & Exhibition (GET 2025)

Conference Paper

1. Burghardt J.A., B. Lecampion, A. Mori, and D.C. Linneman. 2024. "Design of a Meso-Scale Test of a Fracture Thermal Energy Storage (FTES) System." In Proceedings of the 58th U.S. Rock Mechanics/Geomechanics Symposium, June 23-26, 2024, Golden, CO, Paper No. ARMA-2024-0831. American Rock Mechanics Association (ARMA). PNNL-SA-196273. doi:10.56952/ARMA-2024-0831
2. Möri A., J. Naftalski, T. Liardon, M. Talebkeikhah, B. Lecampion, G. Lu, and J.A. Burghardt. 2024. "Experimental Study of Underground Heat Storage via Hydraulic Fractures." In Proceedings of the 58th U.S. Rock Mechanics/Geomechanics Symposium, June 23-26, 2024, Golden, CO, Paper No. ARMA-2024-0540. Westminster, Colorado:American Rock Mechanics Association (ARMA). PNNL-SA-195639. doi:10.56952/ARMA-2024-0540
3. Mathey, Ambroise, Pierre Salome, Möri, Andreas, Lecampion, Brice, “Decimeter-scale Laboratory Investigation of Fracture Thermal Energy Storage”, PROCEEDINGS, 51st Workshop on Geothermal Reservoir Engineering, Stanford University, February 9-11, 2026

Journal Article

1. Hibbard L.E., D. Sirota, M. Ingraham, J. Pope, T. Myers, and J.A. Burghardt. 2025. "Preliminary Observations from a Decameter-Scale Field Test of Fracture Thermal Energy Storage: Initial and Induced In-Situ Stress and its Impact on Fluid Flow." Submitted to Geothermics. PNNL-SA-215629. [In Review] Preprint available at https://papers.ssrn.com/sol3/papers.cfm?abstract_id=5518007.

Software

N/A

Presentations

1. Burghardt J.A., M. Ingraham, Y. Zhang, and B. Lecampion. 11/17/2022. "Development, Monitoring, and Control of Fracture Thermal Energy Storage (FTES) in Crystalline Rock Formations (DEMO-FTES)." Presented by J.A. Burghardt at GEOTHERMICA kick off meeting, Online, Washington. PNNL-SA-180008.

2. Burghardt J.A. 09/28/2023. "Demonstration of Fracture Thermal Energy Storage (DEMO-FTES)." Presented by J.A. Burghardt at SURF Science Program Advisory Committee, Lead, South Dakota. PNNL-SA-190670.

3. Burghardt J.A., and H.A. Knox. 12/09/2022. "Underground Laboratories to Advance Geothermal Energy." Presented by J.A. Burghardt at 1200 Seconds of Science, Online Conference, South Dakota. PNNL-SA-181762.

4. Hibbard L.E., J.A. Burghardt, D. Sirota, Y. Zhang, B. Lecampion, and D.C. Linneman. 12/10/2024. "Design and Operation of a Meso-Scale Fracture Thermal Energy Storage Test." American Geophysical Union Presentation, Washington Dc, District Of Columbia. PNNL-SA-206743.

A Mathey, A Möri, J Burghardt, B Lecampion, “Laboratory Scale Investigation of Fracture Thermal Energy Storage”, Sixth EAGE Global Energy Transition Conference & Exhibition (GET 2025)

Provide a detailed list of all subject inventions, to include patent applications, copyrights, and trademarks:

No subject inventions were generated under this CRADA

Executive Summary of CRADA Work

The DEMO-FTES project sought to demonstrate the thermal efficiency of fracture thermal energy storage (FTES) through numerical simulations, laboratory and meso-scale field tests. A detailed dimensional and scaling analysis was performed to identify key parameters and how they can be most effectively scaled to the laboratory and decameter scale. Numerical simulations were developed and fit to prior hydraulic/thermal tests at the meso-scale testbed at the Sanford Underground Research Facility (SURF). These results were used to design and conduct laboratory tests at EPFL Lausanne and meso-scale tests at SURF.

Laboratory tests were conducted by hydraulically fracturing 25 cm cubic samples of Gabbro under true-triaxial stress conditions. Samples with both a single fracture and three sub-parallel fractures were created. A second production borehole was drilled in each sample and then used for subsequent thermal testing. Thermal tests were conducted at a range of injection rates and temperatures. Both single-cycle and multiple charge-discharge cycles were tested. The temperature distribution on the exterior of the block as well as the inlet and outlet fluid temperatures were monitored. The tests showed that under advection-dominated conditions, the injection rate primarily determines how quickly thermal energy is delivered to the system, while the eventual equilibrium temperature is set by boundary losses and the thermal diffusivity of the surrounding rock. The thermal losses from the exterior of the rock sample were substantial and are not representative of the magnitude of losses that would be expected in a FTES, especially after multiple charge-discharge cycles have heated the surrounding rock mass. The laboratory tests also observed that the injection pressure was dependent on the fluid temperature. Generally, higher fluid temperatures led to higher injection pressures—likely due to thermoelastic effects on the fracture aperature. Laboratory tests also found that when fluid velocities in the fracture were very high a substantial amount of energy could be lost to the produced water because there was insufficient time for it to efficiently transfer to the rock. In these cases the discharge temperatures would initially exceed those of the average rock mass—indicating a high thermal gradient adjacent to the fracture faces. For lower fluid velocities the rock mass was heated more uniformly and substantially less energy was lost to the produced fluid. For future FTES efficiency measurements, operating conditions in this lower-power range are therefore preferable, as they maximise the fraction of energy transferred and retained by the rock.

The meso-scale field tests at SURF used a five-spot pattern of subhorizontal boreholes that had been drilled for the EGS Collab project. At the injection depth the boreholes are separated by approximately 10 meters. The native rock temperature is approximately 27 C. Starting in December 2024 water was injected at 2.5 L/min and ~53 °C into a central borehole. The fluid flowed through fractures that were held open by the fluid pressure (no proppant was used) and was produced from the four surrounding boreholes. Approximately 40-60% of the injected fluid was recovered during this thermal charging phase. Initial injection pressures were ~3800 psi, but gradually rose to 5000 psi within a few weeks. The injection rate had to be lowered to stay within pumping system pressure limits. The pressure continued to rise throughout the experiment, requiring the injection rate to be reduced to 1.5 L/min by the end of January 2025. A significant majority of the fluid was produced from one of the surrounding boreholes. The temperature of the fluid produced from this borehole rose steadily by a few degrees C during the charging phase, indicating likely thermal breakthrough into the production borehole.

A thermal discharge phase was initiated in March of 2025 by injecting ambient temperature water into the outer wells that had produced fluid during the thermal charging phase. Only approximately 10% of the injected fluid was recovered from the central well. The produced water was approximately 32-34 C and gradually declined. Because of the very low production rates the thermal discharging test was terminated after 11 days.

The poor fluid recovery appears to be the result of a combination of existing unfavorable stress gradients within the testbed and stress gradients created by the heating of the rock mass around the central well during the thermal charging phase. Specifically, the stress was initially approximately 300 psi more compressive around the central well than at the outer wells. This made fluid flow relatively easily from the central well to the outer wells, but fluid tended to flow away from the higher stress zone around the central well. The fracture closure pressure in the central well, along with the injection pressure, rose by more than 1500 psi during the thermal charging phase. Meanwhile, there was an increase of only 100-200 psi in the closure pressure surrounding the outer boreholes. This same effect was observed in the laboratory and is believed to be primarily due to thermal expansion of the heated rock mass. Therefore, a key learning of this project is that the changes in the stress field and consequent changes in fracture aperture and transmissivity cannot be neglected in FTES. The fact that the fractures were not propped and instead were held open by the fluid pressure likely make this effect particularly large. The transmissivity of propped fractures would be expected to be much less sensitive to increased compressive stress. Therefore, a key conclusion of the project is that any future thermal tests of FTES must include propped fractures.

Summary of Research Results

Fracture thermal energy storage (FTES) is a concept for seasonal thermal energy storage that utilizes induced fractures to exchange heat with a rock mass. With FTES boreholes are drilled into a low permeability rock mass and then hydraulically connected via induced fractures. Thermal energy is transferred to the rock by injecting hot fluids into one or more wells while the injected fluid is produced from other wells. Then, thermal energy is recovered by reversing the direction of flow while injecting fluid that is initially at a lower temperature than the heated rock mass. Since rock has a high specific heat and relatively low thermal conductivity, large amounts of thermal energy can be stored in a rock mass for long periods of time. This makes this concept very attractive for seasonal storage. FTES has the potential to dramatically lower energy requirements for heating and cooling and improve the resilience of building energy systems. The objective of DEMO-FTES was to determine the feasibility of FTES through numerical, laboratory, and meso-scale field tests.

The technology readiness level (TRL) of FTES was estimated to be 3 because only part of the conceptualized system has been tested experimentally (flow system construction). Other parts of the system, such as the heat transfer to and from the system, have been evaluated only numerically. The DEMO-FTES project sought to advance FTES to TRL 5 during the two-year duration of the project by conducting a thermal storage/production cycle experiment in a realistic geologic setting, but at length and time scales smaller than those expected for largescale commercial applications of the technology.

Prior to DEMO-FTES the most advanced experimental evaluation of the FTES concept was a study by Ramstad et al. (Ramstad et al. 2007). This study demonstrated construction of the flow system but did not include a thermal test. This field test consisted of a series of three field tests in Norway, using water only or water and sand for proppant. A similar five-spot pattern to that employed by Hellström and Larson (Hellström and Larson 2001) was used. The field tests showed that production rates from the central well while fluid was injected into the outer wells was lower than expected and represented the greatest challenge to economical production.

Below is a summary of the work conducted and major results of each task of the project. Each subsection corresponds to a task named in the project statement of work.

1.0 Work Package 1: Dimensional analysis, scaling, and numerical modelling Dimensional analysis and scaling

1.1 Dimensional analysis and scaling

The first task involved dimensional analysis (Task 1.1) and numerical modeling (Task 1.2) to design the field test. For Task 1.1 a rigorous dimensional and scaling analysis was conducted to ensure that the decimeter-scale test would be informative to larger scale commercial FTES operations. This work was published in a paper at the 2024 American Rock Mechanics Association (AMRA) Symposium (Burghardt et al. 2024). This work identified 14 key system design parameters and their approximate values in a full-scale system. These were translated into a set of dimensionless quantities using the Buckingham-Pi theorem. The physical meaning of each parameter was identified and a set of design parameters for the meso-scale experiment were derived that maintain, as closely as possible, the value of the dimensionless quantities.

1.2 Numerical modeling

In this subtask, numerical models were used for three purposes: 1. Before field experiments, numerical modelling can be used to estimate fracture size, shape and properties based on previous data from the EGS Collab experiment and then predict thermal hydrological behaviors of the fracture system with hot water injection/withdrawal, therefore, help to design the experiments (e.g., to decide the duration of the cycles based on the flow rate the pump can provide, and the estimated fracture properties); 2. After the field experiment, to estimate the system properties during the experiment (as the size and shape of a fracture could change over time), and understand why system performance is different than what has been predicted, i.e., to help understand the meso-scale test; and, 3. To model the lab experiments and estimate fracture properties and storage efficiency. Ultimately, the experiment and numerical models could shed light on the processes and uncertainty happening during fracture activation and help understand the scaling between lab and field test, and finally, the design and optimization of potential fracture thermal energy storage systems.

1.2.1 Simulation Software

TOUGH (Transport Of Unsaturated Groundwater and Heat) is a suite of numerical simulation software tools developed by Lawrence Berkeley National Laboratory (https://tough.lbl.gov/). It was designed for modeling nonisothermal flows of multicomponent, multiphase fluids in multi-dimensional porous and fractured media (https://tough.lbl.gov/). Among the various Equation-of-State (EOS) Modules, the EOS1 module was specifically developed for and widely used in geothermal applications, providing a description of pure water in liquid, vapor (gas) or two-phase conditions.
iTOUGH2 (inverse TOUGH2) (https://tough.lbl.gov/software/itough2-software/) is a computer program that provides inverse modeling capabilities for the TOUGH codes, with enhanced capabilities (Finsterle, 2023). iTOUGH2/EOS1 is used in all the analysis described below.

1.2.2 Modelling of Meso-Scale Field Test

The fracture used for the meso-scale field test was the fracture created during the EGS Collab experiment (2022). First, a model was built and calibrated to match the thermal test measurements between June 17 and August 4, 2022. Since the field tests were done in

2024/2025, it is reasonable to assume that the properties of the fracture (i.e., size and shape, permeability distribution) will be different after its partial closure and re-stimulation in 2024. The same model domain with different model properties were used to match the data obtained from the field tests in 2024/2025.

1.2.2.1 Fracture model calibration

A plane discretized in 2D, with a uniform thickness in the 3rd dimension was built to represent the fracture and low permeability rock matrix around it. The interpreted fracture (i.e., the large purple disk shown in Figure 1) is assumed to be ellipsoidal. It is represented by a user-specific region with varying permeability (Finsterle et al. 2023). The location and size of this region is parameterized and thus subjected to parameter estimation by inverse modeling using the data from Figure 2. In addition, the key parameter (non-geometric) affecting the fluid flow in the fracture is the transmissivity. Since the thickness of the model is fixed, the permeability of the fracture will be estimated. The fracture region comprises multiple discretized elements, with a smooth function describing the transition of permeability between the fracture and the background domain (rock matrix) as a function of distance from the center of the fracture. The heat exchange between fluid flow in the fracture and rock matrix is modelled using the semi-analytical heat solution (Zhang et al. 2011).

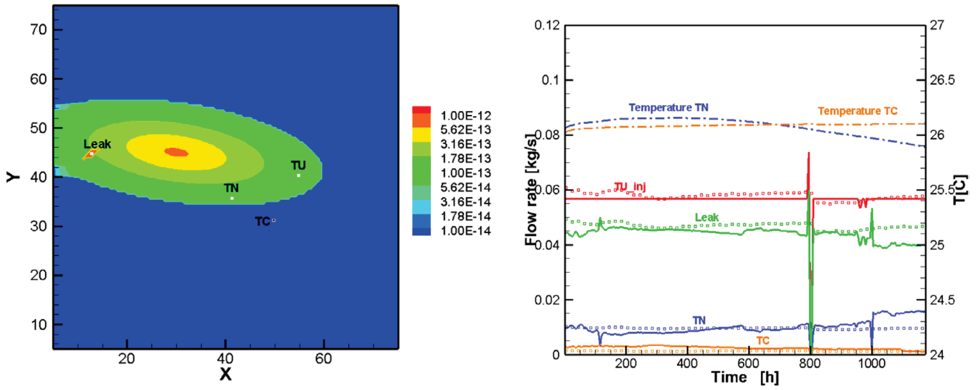

Figure 1 Fracture model calibrated from the 2022 Collab experiment: a) calibrated fracture shape and permeability; b) History match for temperature and flow rate for the Collab experiment.

The natural fracture (indicated as leak) as shown in Figure 1 is not modelled explicitly but its effect is modelled by modelling an effective intersected area (of a line shape) between the main fracture and the natural fracture. The intersection is assumed to be at the atmospheric pressure during the tests.

Using the calibrated model, a number of scenarios with different length of loading/unloading periods were investigated. Among those, the scenario consisting of 50 days loading and 50 days unloading has the best thermal performance. It is slightly preferable to inject into both TN and TC wells, although the benefit is not significant.

1.2.2.2 Matching field test

Model calibration was mainly focused on the Phase I test, in which hot water was injected through TC and produced out of TN and TL from approximately 12/13/2024, 20:00:00 to 02/23/2025.

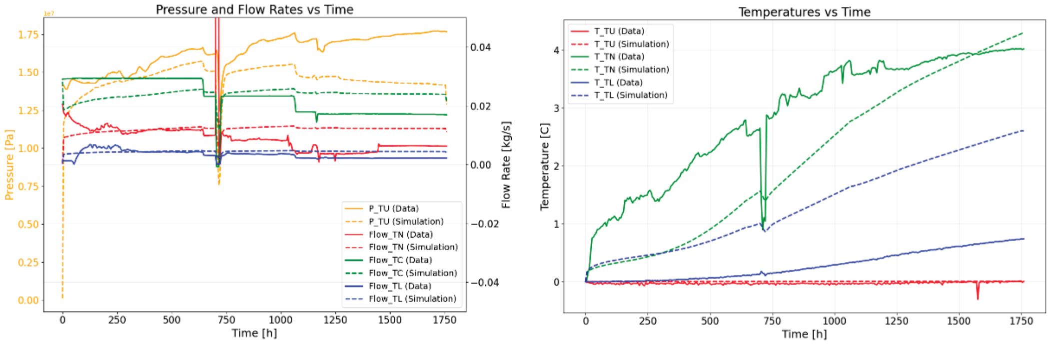

Figure 2. History match for the field test between 12/14/2024, 00:00:00 to 02/23/2025, 11:00:00.

Figure 2 shows the history matching of the field test between 12/14/2024, 00:00:00 to 02/23/2025, 11:00:00. During this period, hot water was injected through TC and flew out of TN and TL. The pressure was prescribed at TC, and flow at TC was used as an observation to be matched to the actual flow. Injected hot water gradually heat up the rock around it, causing its thermal expansion, and as a result, reducing fracture spacing and therefore, fracture permeability. In the test, the injection rate at TC was decreased after approximately 30 days to mitigate a substantial rise in injection pressure. Because the model did not include the process of reduced fracture permeability, the simulated flow at TC was not reduced because it reflects the actual injection pressure and an unchanging permeability. Inaccurate flow rates in the model results in mismatch in temperature as well. In addition, heterogeneity in stress field was not captured by a model that does not simulation geomechanics. The field test clearly demonstrated the complex coupled processes in a fractured system, and importance of understanding them, including them in the predictive models.

1.2.3 Modelling of Lab Experiments

The lab experiments contain two sets: single fracture tests and three fracture tests. As the data were obtained at the end of the project, effort was main made to model the first single fracture experiments, performed on April 16, 2025.

The main advantage of a lab experiment is that it is well controlled, and the exact fracture location can be measured. A 3D model was built using the actual sample size. The fracture plane was estimated based on visual estimates of the actual fracture, while the actual size was a parameter for model calibration. The model was modified a few times to capture the details of the system, including: injection/production well size, well material, and sample boundary conditions (i.e., how the sample was separated from outside). Temperature sensors were located both at the production well bottom, production well outlet, and sample surface. The initial temperatures at these locations vary between 19.7°C (production well outlet) and 22.5°C (some of the surfaces). There is no known process to explain the low temperature at the product well outlet. For history matching effort, the injected flow rate and temperatures were used as model input. The uncertain parameters (adjusted to match the model output to measurements) include fracture size, location and hydraulic properties, thermal properties of the well filling material (between the injection pipe and rock sample), rock sample, the thin layer of resin outside the sample to prevent flow from the fracture, and the box that contains the sample. The model output includes the temperature change (compared to initial temperature) at each measured locations and injection pressure, which were matched to actual measurements.

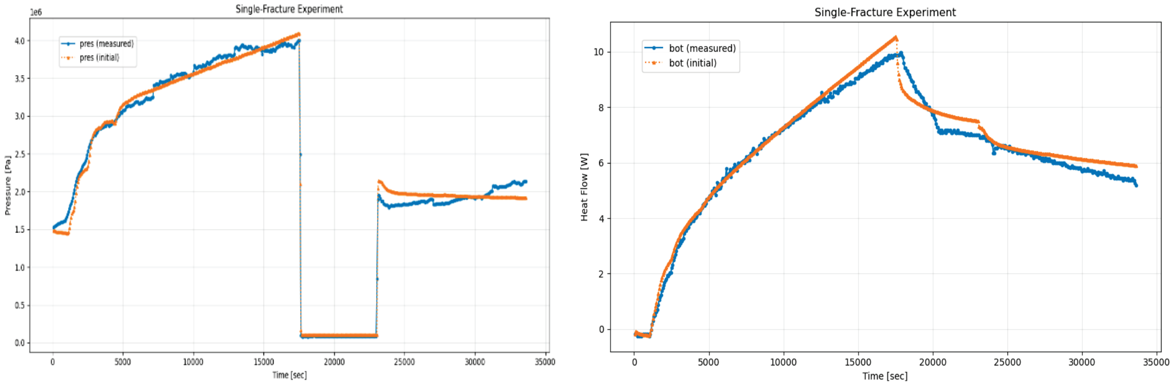

Figure 3. History match for the single fracture lab experiment performed on 4/16/2025.

The experiment consisted of three period: hot water (75°C) injection for about 5 hours (17615 seconds) at 5mL/min; No injection for about 1.5 hours; Final room temperature (22°C) injection for about 3 hours at 5mL/min. The pressure data plot in Figure 3 clearly shows a much higher temperature increase due to hot water injection compared to cold water injection. This could come from the thermal expansion of the rock due to significant temperature increase, and therefore, reduction in fracture aperture, and fracture permeability. In the model, an estimate was made for the aperture reduction, permeability was modelled as a function of the aperture (power law) to match the pressure. The aperture has a 30% reduction after hot water injection and permeability had an about 60% of reduction.

The lab experiment highlights the importance of understanding relevant processes (e.g., thermal conduction, advection, thermal expansion, boundary conditions etc) in energy storage projects.

2.0 Work Package 2: Laboratory demonstration of FTES

This research project aims to quantify the potential of FTES in terms of long-term thermal storage performance, expressed through metrics such as the Thermal Recovery Factor (TRF). In this report, TRF is used as a project-specific indicator of heat recovery, defined for the purpose of FTES laboratory and modelling studies. It should not be interpreted as a generic thermodynamic efficiency but rather as a contextual measure that allows comparison of heat recovery across experimental conditions. The DEMO-FTES project includes contributions from U.S. partners (PNNL, LBNL, SNL) and Switzerland (EPFL) within the framework of the GEOTHERMICA Era-Net and Joint Programming Platform Smart Energy Systems (JPP SES) – Joint Call 2021. This report focuses on the laboratory investigations performed at EPFL.

In this study, fractures were created in 25 cm cube specimens of crystalline Gabbro and Lanhélin Granite using controlled fracture initiation. Two specimens were prepared with a single fracture, while a third contained three parallel fractures. Outlet wells were then drilled. Thermal loading and unloading experiments were conducted by circulating hot or cold fluids between the injection and outlet wells under various flow-rate conditions. Inlet and outlet fluid temperatures, as well as temperatures at several surface locations on the specimens, were monitored continuously.

These laboratory experiments demonstrate the feasibility of the fundamental physical processes underlying FTES—namely injection, storage, and retrieval of thermal energy—and provide a comprehensive dataset to support the validation and development of numerical models. However, the energy recovered during these finite laboratory systems (measured by the Thermal Recovery Factor -TRF) are strongly influenced by radiative heat losses from the sample surfaces. As such, the reported TRF values should not be interpreted as representative of field-scale performance but rather as controlled laboratory demonstrations of the principles of FTES mechanisms and as essential data for modelling efforts.

2.1 Creation of fractures

The propagation of hydraulic fractures was performed in a true triaxial press developed at EPFL Geo-Energy lab. The apparatus enables the independent control of the three principal stresses applied to the cubic rock samples through three pairs of opposed piston arrays. Each array is composed of nine pistons arranged in a 3 × 3 grid, housed within a solid steel frame. The arrays press onto the sample faces and apply normal stress, ensuring a uniform confinement over the surface. The confining pressures are generated by three GDS Pressure-Volume Controllers (200 mL), each driving one pair of piston arrays. The system is operated through a LabVIEW interface, which maintains the applied pressure constant during the entire fracturing process. In all configurations, the two horizontal stresses are equal ($\sigma_1 = \sigma_2$) and greater than the vertical one (σ_3), so that the fracture propagates preferentially in a horizontal plane. The samples used are 25 cm cubes displaying variations of about ± 2 mm in their edge's length. Between the pistons and the sample are placed 2 cm thick platens, which still ensure homogeneous transmission of the load while providing the interface for instrumentation. The platens contain electrical feedthroughs that allow the cables from acoustic sensors to exit the press safely. The injection line passes through the top platen and connects to the injection tool inside the central well of the sample. To inject high viscosity fluids, a bladder-like interface vessel is used to transmit the injection rate from the pump filled with distilled water to the high-viscosity fracturing fluid (see Figure 4 right).

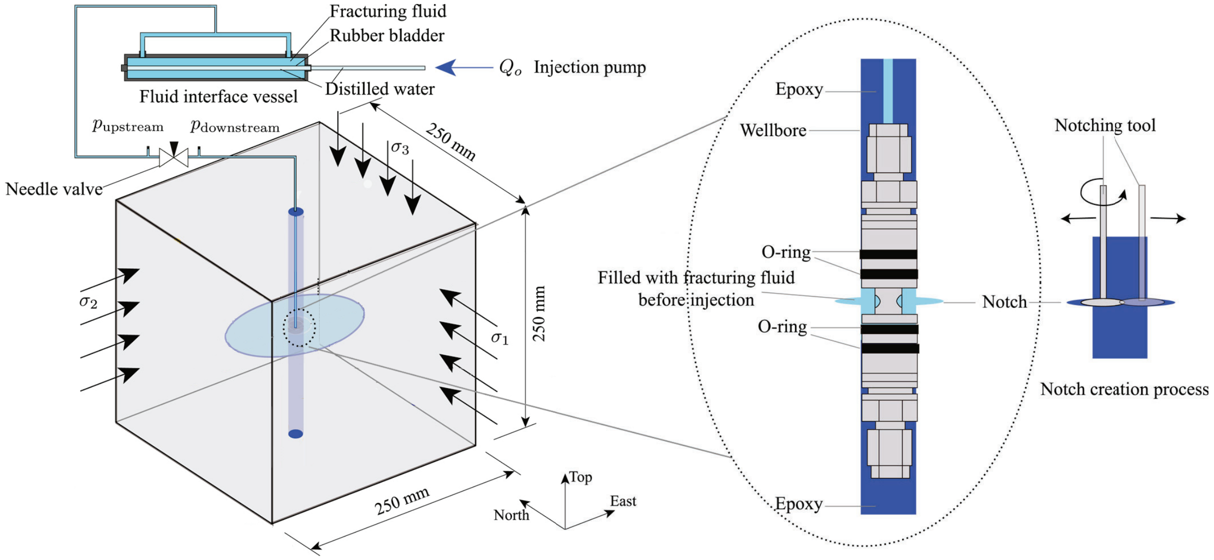

Figure 4 Left: Schematic of the 25-cm cubic rock specimen in the triaxial. Nine pistons arranged in a 3×3 array apply normal stresses on each face, ensuring uniform confinement. Right: Zoom on the injection tool used for single-fracture experiments. Once positioned at the notch depth, the surrounding well is filled with epoxy to isolate the injection volume and withstand high pressure. (Figure modified from (Liu and Lecampion 2022))

Monitoring during the fracture propagation stage relied on an array of active and passive acoustic sensors integrated into the experimental setup. All sensors are mounted within the platens placed between the sample faces and the piston arrays. Each sensor was pressed against the rock surface using a spring mechanism to ensure constant contact, and a thin layer of couplant was applied between the sensor and the sample to improve coupling. The cables from the sensors passed through electrical feedthroughs in the platens and were connected to the acquisition system outside the press (see Figure 5 for a schematic of the sensor layout).

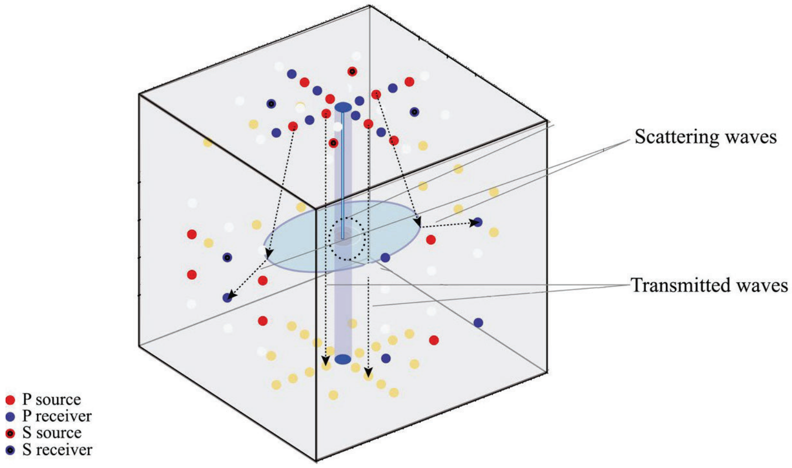

Figure 5. Schematic layout of the position of the active and passive acoustic sensors embedded in the platens. Active transducers allow repeated scans to monitor fracture opening and propagation, while passive sensors continuously record acoustic emissions from microcracking during fracture propagation. (Figure modified from (Liu and Lecampion 2022))

The passive sensors recorded the acoustic emissions generated spontaneously by microcracking and fracture propagation. The high-frequency data were used to locate events in three dimensions and to construct AE catalogues showing the spatial and temporal evolution of the fracture using the SIMORGH AE processing software. These catalogues provide a complementary view to the active measurements, identifying the sequence of microcracking and the regions of highest activity. They were also particularly useful for detecting signs of epoxy debonding or leak initiation before macroscopic fracture propagation occurred.

2.1.1 Sample preparation & well completion

Before presenting the results, it is important to clarify that the confining stresses and injection parameters used in these experiments were chosen specifically for the needs of the laboratory setup, not to reproduce the exact conditions expected in a real FTES system. The confining stresses were selected to be representative of stress typically encountered in intermediate crystalline formations (up to 800 meters depth), targeting stress regimes for which the vertical stresses is lower than the horizontal stresses such that horizontal fractures are created. Although the absolute magnitudes in the experiments were often higher than the in-situ values typically found at 100m, these elevated confining stresses were necessary for experimental repeatability, notably to ensure the hydraulic containment of the high-pressure fluid injection and allow the hydraulic fracture to propagate in a planar fashion. In other words, the absolute stress magnitudes should not be interpreted as representative of shallow-depth crystalline rock, but rather as values that make the experiment work reliably.

Similarly, the injection programme was designed to produce slow-propagating fractures (from roughly 10 seconds to several minutes), which allows to track fracture growth with our acoustic sensors. This approach follows standard practice in laboratory hydraulic-fracture studies, where higher viscosities and carefully controlled rates are used to slow down propagation and allow detailed monitoring ((Warpinski et al. 1982; Feng et al. 2024; Detournay and Garagash 2003; Lecampion and Desroches 2015)).

Overall, the parameters used here should be seen as experiment-driven choices that allow stable fracture creation and high-quality measurements, rather than direct analogues of field FTES operating conditions.

The injection wells were cored vertically through the entire height of the samples, with diameters ranging from 1.6 to 2 cm, depending on the specimen. Each well was later completed using epoxy resin to seal the annular space surrounding the notch and mechanically support the internal tubing. The injection fluid was delivered through a stainless-steel tube (1.6 mm in internal diameter) inserted into the completion and connected to the external circuit via the top platen.

2.1.2 Single-fracture configuration

For the single-fracture experiments, the completion tool consisted of a metal cylinder (3–5 cm long, same diameter as the well) containing a central injection line that exited laterally through a small hole in its wall. Four O-rings were placed above (2) and below (2) this injection opening to isolate the targeted interval from the rest of the well. Once the assembly was positioned, the remaining void was filled with epoxy resin, which, once cured, provided a strong mechanical seal able to sustain high pressures during injection. In a few cases, some epoxy is suspected to have infiltrated the injection space, but no fracturing fluid was ever observed leaking into the surrounding well during operation, confirming the overall tightness of this configuration.

2.1.2.1 GABB-08 sample

Hydraulic fracturing of block GABB-08 was carried out under the following confinement applied by the piston arrays: 10 MPa along the East West axis, 10 MPa along the North South axis and 8 MPa along the Top Bottom axis. A notch was machined halfway down the well, that is at 12.5 cm below the top face along the well axis. Glucose was used as the fracturing fluid. A first attempt was made with an injection rate of 0.06 mL/min. Pressures were recorded on the line immediately upstream of the block and reached a peak of 62 MPa. However, no fracture trace was visible on any face after the experiment. From the pressure and acoustic emissions that were recorded, we estimated that epoxy infiltrated the notch during sample preparation and blocked the injection path. During the first attempt, only the epoxy plug inside the injection line failed locally. A second attempt was then performed at 0.1 and 0.2 mL/min under no confinement (the sample was not placed back in the triaxial frame) after cleaning and resetting the completion tool. In this case, the pressure rose to a peak of 68 MPa and the fracture propagated. Those pressure curves are displayed in Figure 6.

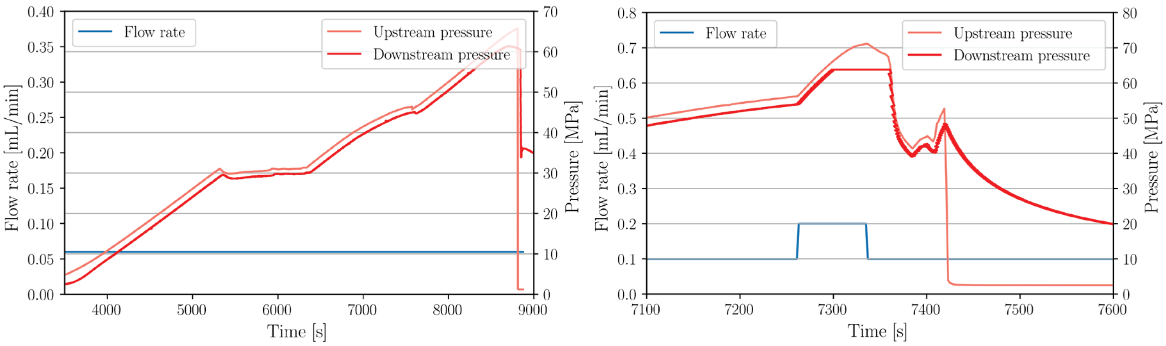

Figure 6. Pressurization record of the initial fracturing experiment for GABB-08. Dark red is the upstream fluid pressure and light red is the downstream fluid pressure given on the left scale. The blue line is the fluid flow rate, shown on the left scale. A first breakdown is observed when the pressure reaches ~ 62.5 MPa. Most likely, the epoxy fixing the completion tool into the wellbore leaked into the notch. At the measured high pressure, this clog is fractured. We then observe a second pressurization phase up to ~ 45 MPa, where the fracture initiate.

We recorded both active and passive acoustics during these attempts and the coordinates of the visible fracture were later mapped on photographs of the block faces. The mapping of the external trace can be shown alongside a picture of the sample in Figure 7.

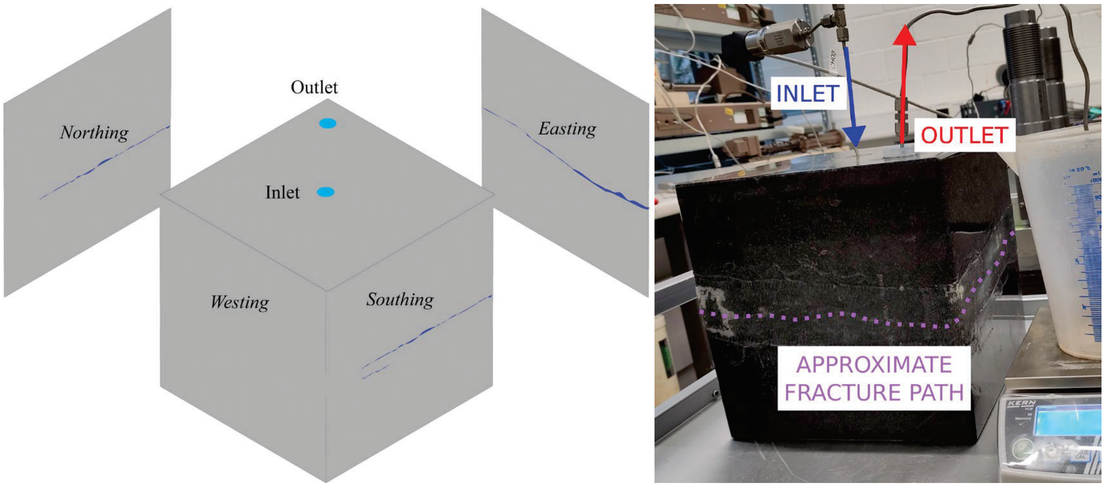

Figure 7. Left: representation of the GABB-08 apparent fracture. Right: Sample with inlet and outlet well and sealing of the fracture.

2.1.2.2 LANH-02 sample

A Lanhélin granite sample previously fractured in the laboratory was re-used for single fracture thermal experiments during this project. For fracturing the LANH-02 sample, the confining stresses were set to 5 MPa along the East West axis, 5 MPa along the North South axis while no stress was applied along the Top Bottom axis. The notch was again at 12.5 cm from the top face along the well axis. Fracturing was performed with a silicone oil of viscosity 100 mPa·s at an imposed injection rate of 0.06 mL/min. The fracture propagated up to 3 of the 4 faces of the block. A production well was then drilled to enable a closed-circuit configuration during the thermal tests. This outlet well was located in a corner of the top faces of the sample (10 cm from the inlet well), and the bore (core diameter 1.6 cm) was cored until it intersected with the fracture. The production well was completed with a completion tool and epoxy, and the external openings were sealed with epoxy and glass fibre. Figure 8 displays the fractured sample with its injection and outlet wells. Leaks along the external opening of the fracture developed later in the campaign and with lower frequency than in the previous block, which is consistent with its higher transmissibility and the lower hydraulic load during operation.

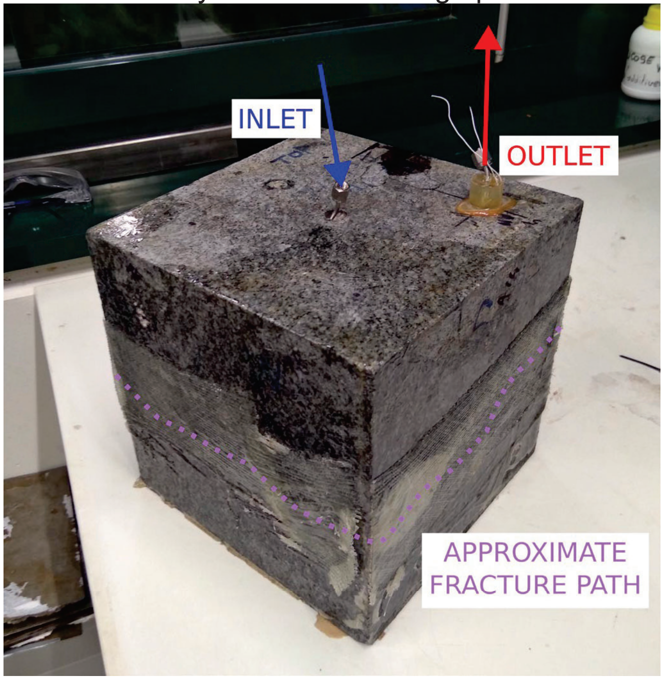

Figure 8. LANH-02 sample with inlet and outlet well and sealing of the fracture with epoxy and glass fibre.

2.1.3 Three-fractures configuration – first design

To allow the creation of multiple fractures within a single sample, a packer-like system was first developed. The setup consisted of a single injection cylinder that could be positioned at different heights inside the injection well by stacking it either on top of, between, or below two additional dummy cylinders. These dummy cylinders served only for alignment and support, enabling the injection port to be placed at the desired depth corresponding to the target fracture plane. The entire column was compressed from above by an external piece applying axial load, which deformed the O-rings of the injection section to seal it against the well wall. While conceptually simple, this configuration required substantial compression to maintain tightness. Bench tests conducted at 5–6 MPa inside a fake metallic well demonstrated that such stress levels would apply significant stress to the inside of the well as shown in Figure 6. This potential for rock damage and repetitive O-rings failure under high load led to the abandonment of this design before any fracture propagation experiments were carried out.

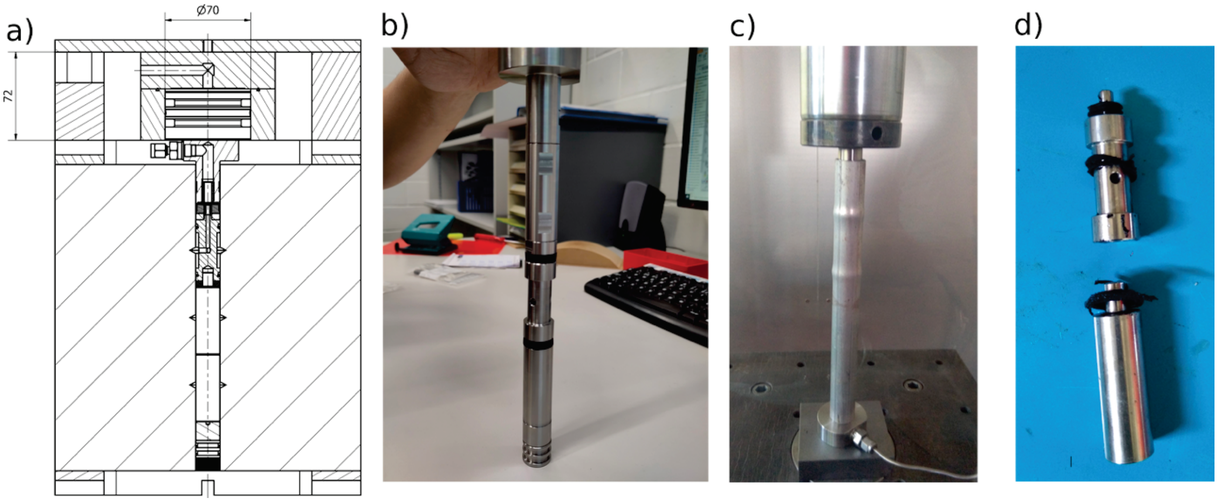

Figure 9. Initial design for a multi-level injection tool. It is composed of 3 modules, 1 for injection and 2 for positioning and support. By moving these modules the injection line can be placed in front of the notch made at different heights in the well. The seal around the injection line is ensured by deforming the 2 O-rings (in black) following a packer-like design.

2.1.4 Three-fracture configuration – second design

A second idea was then developed, based on three shorter injection cylinders preassembled into a single column and glued together with epoxy before insertion into the well. This well completion design is presented in Figure 7. Each section to be fractured contained its own injection port, spaced by approximately 7 cm along the axis, to target three distinct fracture planes. The injection ports were placed in front of axisymmetric notches created to help fracture initiation. Once the column was inserted, additional epoxy was poured into the remaining space to secure the assembly. Although this design avoided the need for mechanical compression, the limited spacing between the cylinders meant that the epoxy layer separating them was thin. During injection at high pressure, partial unbonding occurred locally, which seems to have led to some cross-leakage between injection levels during the fracturing (as we discuss later). Future designs should therefore rely on shorter injection sections and thicker epoxy layers to ensure complete isolation between adjacent fractures.

After the creation of the fracture(s), we have removed and replaced this injection in order to ensure proper zonal isolation between the three fractures. Such a completion design has the added advantage of allowing to perform FTES circulation experiments in one, two or three fractures at a time.

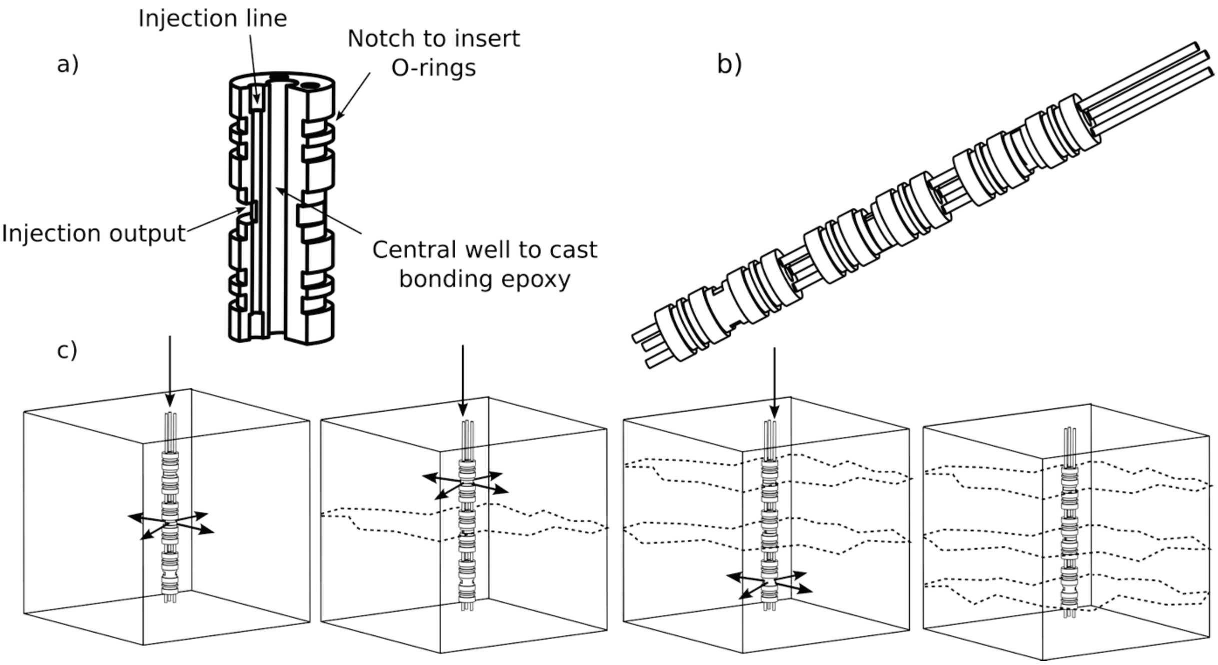

Figure 10. Second design for the multiple fracture completion tool. This design consists of three distinct injection modules placed on top of each other. Each module lets 2 injection lines through and is open on the third. The modules are held in place by gluing the injection tubing with epoxy. This allows to inject fluid at the top, middle or bottom via three separate injection lines.

2.1.4.1 Three fracture sample: GABB-11

The third gabbro cube (25 cm) was prepared with a central vertical well and three notches at 7.0 cm, 12.5 cm, and 18.0 cm below the top face along the well axis. Confinement was applied with piston arrays on all six faces such that the two horizontal components were equal and the vertical component was smaller ($\sigma1 = \sigma2 > \sigma3$), to promote horizontal fracture growth. The multi-level injector (see Section 2.2) allowed for separate injection in front of each notch. The fracturing fluid used for those injections was a glucose solution of viscosity ~65 mPa·s at 20 °C. The injection used the interface vessel described in Materials & Methods (flow imposed on the water side and transmitted to the bladder-contained glucose). The confining stresses and injection programmes are reported below for each attempt. The goal was to inject sequentially in the three injection lines starting by the middle one to maximize symmetry of the placed fractures. We describe below the different fracturing attempt.

First injection sequence (24 May 2025): Injection in the middle line.

The stresses were set to 10 MPa for the horizontal and 5 MPa vertically. After a short stabilisation period (minor leaks and pump issues during the first hour), injection proceeded with only the injection line leading to the middle port open. The injection rate and pressure (recorded immediately at the top of the block) are shown in Figure 11. A first injection (from t ~ 3,252 to 6,400 s) was conducted at 0.05 mL/min, followed by a second one (t ~ 6,500 to 7,900 s) at 0.2

mL/min. After the experiment, the block was lifted out of the frame to be examined. No fracture traces appeared on any of its external faces and no glucose was observed at either end of the injection well. Given the strange pressure evolution and the absence of any external leakage, we inferred that the experiment had likely resulted in a local debonding around the completion/epoxy and the emergence of internal communication between the different injection levels within the well. The accompanying AE catalogue for this attempt indeed showed events clustering along the wellbore consistent with the interpretation of fluid debonding of the epoxy along the completion of the injection well (see Figure 14).

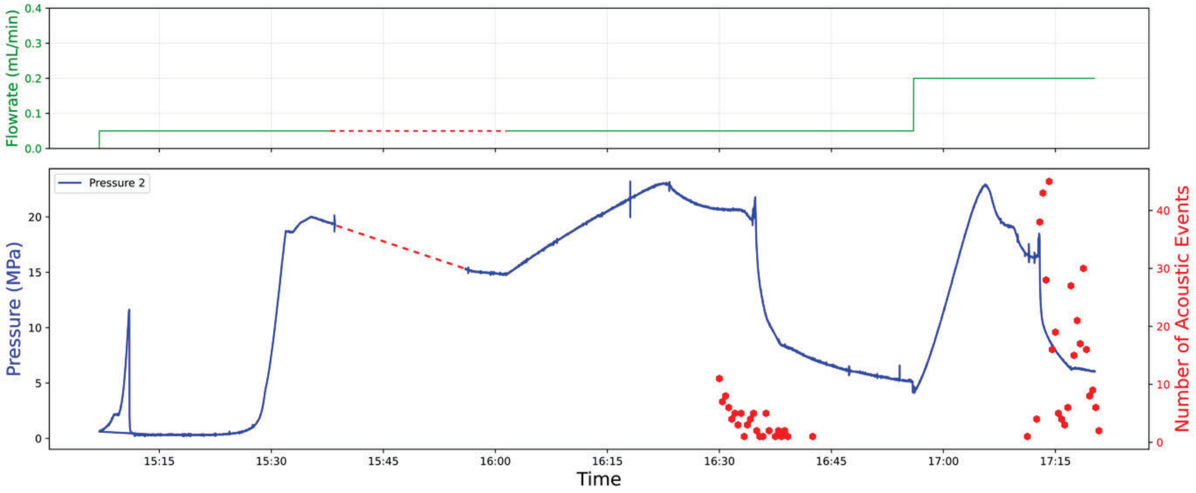

Figure 11. Injection rate and pressure evolution during Attempt 1 (injection in middle port) of the three-fracture experiment. The dashed red line corresponds to a loss of contact between the computer and the pumps/pressure sensor.

Second injection sequence (17 June 2025):

Following the assumption that the three injection lines were most likely hydraulically connected we adjusted our protocol. We decided to inject simultaneously in all three lines. Our expectation was to propagate a fracture in the weakest of the three points of the well in front of the injection lines. In the hope to reduce the connectivity between the injection points, we increased the horizontal confinement to 17.5 MPa to confine as much as possible the likely debonded interface between completion and the rock. The vertical minimum confinement was kept at 5MPa. The injection pressure evolution is displayed in Figure 12. A first injection phase (from t = 0 to 6,800 s) was performed at 0.05 mL/min (with brief early steps at 0.1 and 0.5 mL/min to gain time). Given the low pressure reached during that phase and the lack of a clear pressure peak, we increased the injection rate to 0.2 mL/min (from t = 6,801 to 10,300 s). This gave a truly clear pressure peak and roll-over that we interpreted as the propagation of a fracture. A third injection (from t = 10,400 to 12,000 s) was made at 0.4 mL/min to further open the created fracture. After this, as a test, two short high-rate pulses were imposed at 5 and 1 mL/min. Even though we assumed that a fracture was connecting the injection lines to the outside, the short high-rate pulses still produced substantial pressurisation of the injection network. This told us that despite the inter-connectivity, high injection rates would allow us to pressurise the injection line to propagate other fractures. This was consistent with a narrow connection between injection levels through which our injection fluid could only circulate at low flow rates.

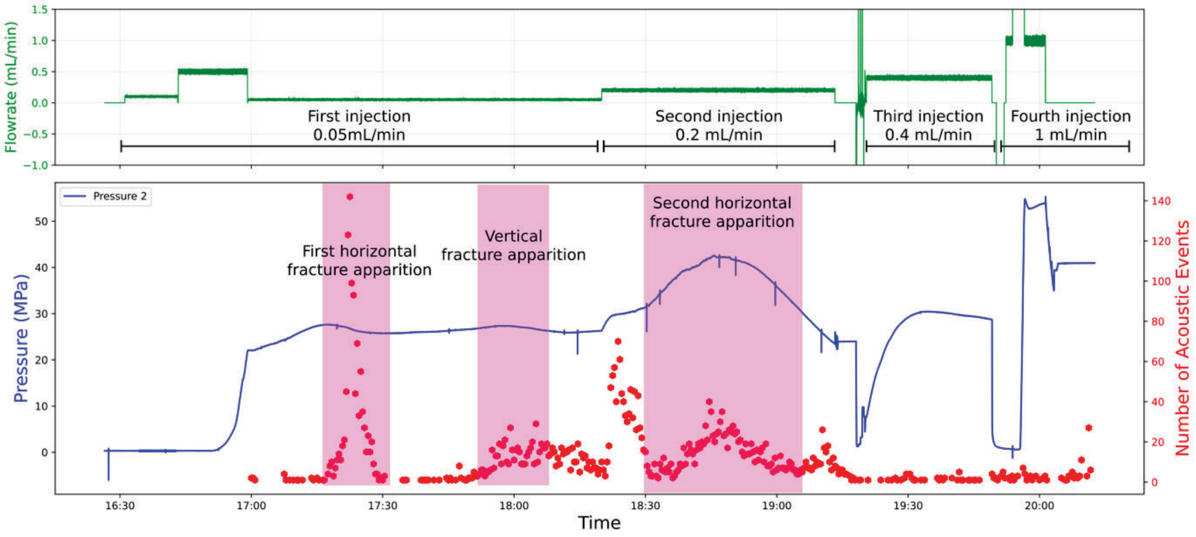

Figure 12. Pressure evolution during simultaneous injection in all three ports (Attempt 2). A distinct pressure peak at the end of the first injection indicates successful propagation of a fracture at the bottom level, later confirmed visually and with the AE catalogues.

After the experiment, the sample was once again lifted out of the frame and examined. A fracture could be clearly seen on the external faces of the block at the height of the bottom notch. Moreover, glucose had stained the plattens pressed against those faces. The AE catalogue for this attempt (see Figure 15) did show a final planar horizontal front at the bottom notch. The AE catalogue also showed that before the final fracture propagation, other fractures had propagated through the sample.

Third injection sequence (24 June 2025):

With the hypothesis developed at the end of the previous attempt, we decided to inject in the top and then in the middle lines. Using higher injection rates, we believed we could pressurise each line independently. Given the higher flowrate, the propagation time of the fractures was going to be much shorter than for the previous experiments. Therefore, we decided to only record the passive acoustic data, to have a continuous recording uninterrupted by the active emissions. We applied the same confinement parameters (17.5 MPa in the North/South and East/West axis and 5 MPa in Top/Bottom axis). For the top line, a first phase (from t = 0 to 1,800 s) was run at 0.5 mL/min, followed by a second phase (from t = 1,800 to 2,200 s) at 1 mL/min. For the middle port, a first phase (from t = 2,200 to 3,340 s) was run at 1 mL/min, followed by a second phase at 2 mL/min. After the experiments, fractures were visible at both depths by surface traces and by glucose marks on several platens at the corresponding heights. After injecting through the top line glucose could be seen exiting the middle line, directly demonstrating inter-line linkage within the completion assembly.

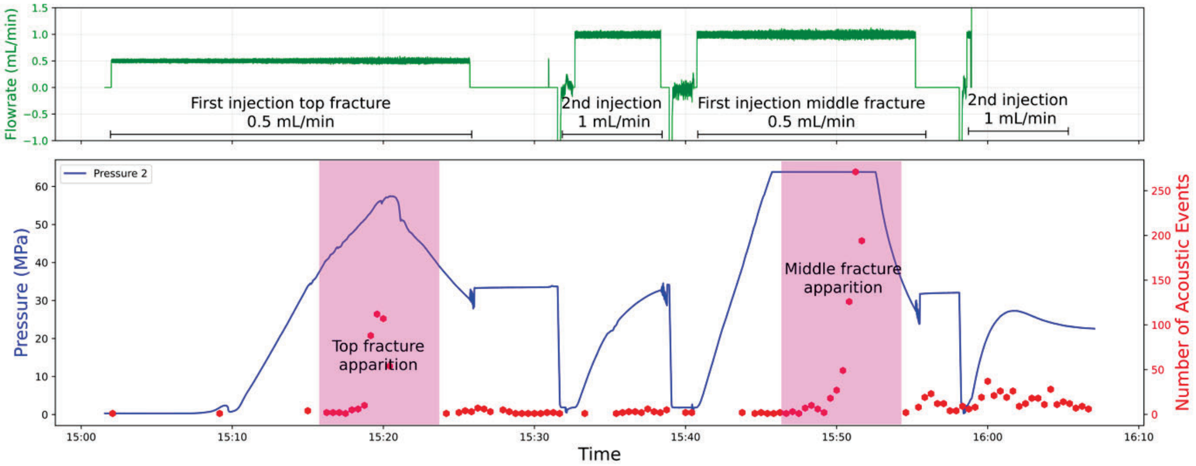

Figure 13. Injection pressures for the high-rate sequential injections performed in Attempt 3. Clear breakdown signals are visible for the top and middle ports, consistent with the two fractures observed afterwards. (Note: the plateau appearing around 15:45 is caused by the pressure gauge reaching its upper limit and does not reflect the actual pressure of the system.)

Table 1. Summary of the injection and pressure parameters for the different hydraulic fracturing experiments

Injection	*Horizontal stress (σ1 & σ2)*	*Vertical stress (σ3)*	*Injection rate (mL/min)*	*Measured injection pressure range (MPa)*
GABB-8 First injection	*10 MPa*	*8 MPa*	*0.06*	*0-62*
GABB-8 Second injection	*0 MPa*	*0 MPa*	*0.1 0.2*	*0-68*
LANH-02	*5 MPa*	*0 MPa*	*0.06*	*No data*
GABB-11 First injection	*10 MPa*	*5 MPa*	*0.05 0.2 (end)*	*0-23*
GABB-11 Second injection	*17.5 MPa*	*5 MPa*	*0.05 0.2 0.4 (end) 1 (end)*	*0-40*
GABB-11 Third injection (Top)	*17.5 MPa*	*5 MPa*	*0.5 (first) 1 (second)*	*0-55*
GABB-11 Third injection (Bottom)	*17.5 MPa*	*5 MPa*	*0.5 (first) 1 (second)*	*>60 (sensor malfunction)*

2.1.5 Hydraulic fracture growth imaging

For each attempt, a passive AE catalogue was calculated using SIMORGH software developed in the lab by Dr. Momeni. They are shown in Fig 3.7, 3.8 and 3.9. The catalogues are plotted in a right-handed laboratory frame (x: west→east; y: south→north; z: bottom→top) and coloured by event time to visualise the propagation of each fracture. Qualitatively, the highest counts of acoustic emissions cluster around the main pressure peaks of each injection sequence as shown in the plots of Figure 11, Figure 12, and Figure 13. In the second attempt, the catalogue (Figure 15) reveals a predominantly planar horizontal front at the depth of the bottom injection line, preceded by a small, less planar horizontal cluster and a vertical cluster aligned with the wellbore; these precursors occur before the final planar fracture and can be associated with smaller peaks seen in the pressure evolution. During the injection sequence #3, compact clusters of acoustic events are clearly visible at the depths of the top and middle injection lines and coincide with the timing of the two injection pairs.

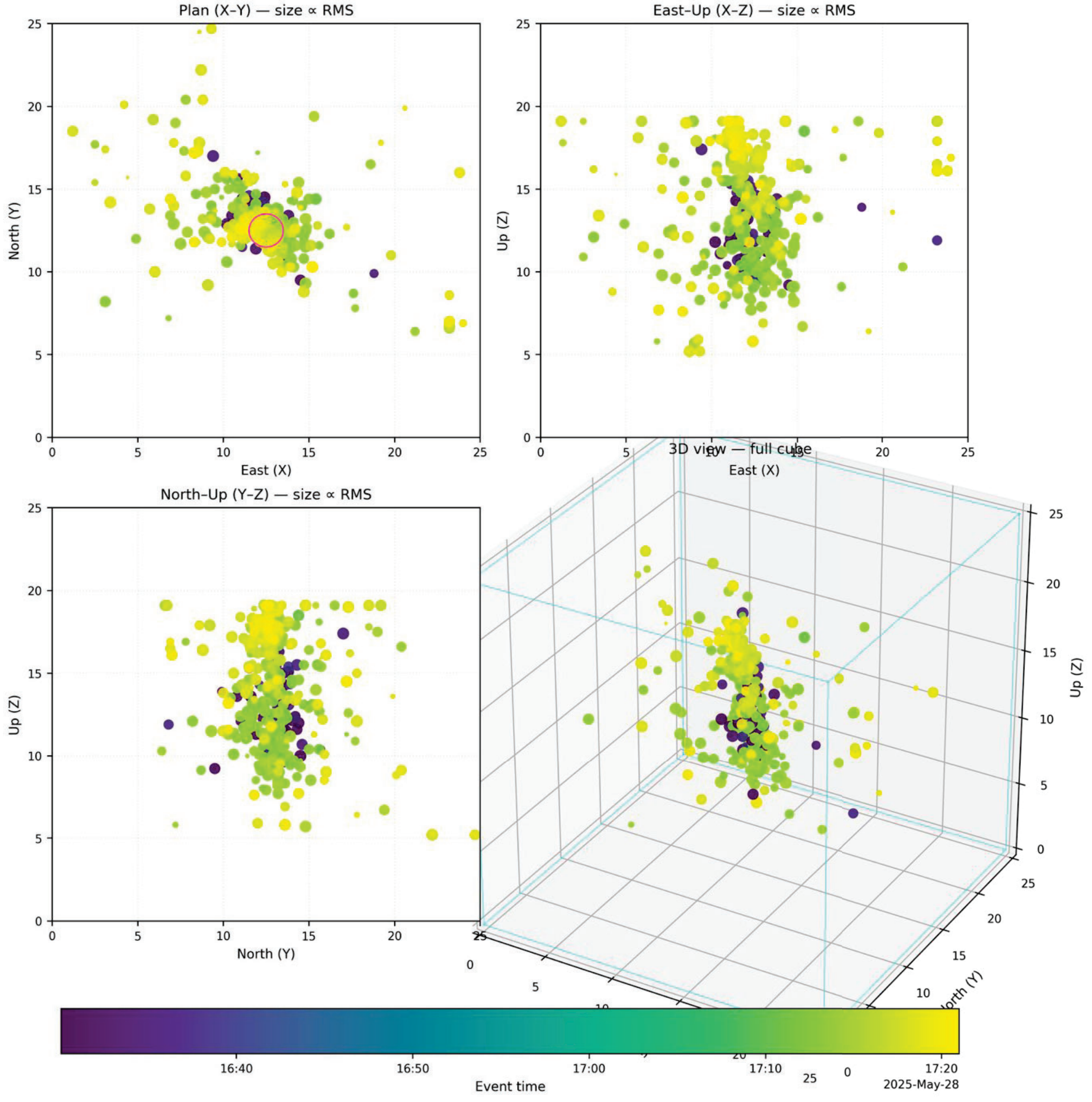

Figure 14. Acoustic emission events recorded during injection sequence #1 plotted in the laboratory coordinate system. Events concentrate along the wellbore, supporting the interpretation of local debonding along the completion of the injection well rather than hydraulic fracture growth within the block.

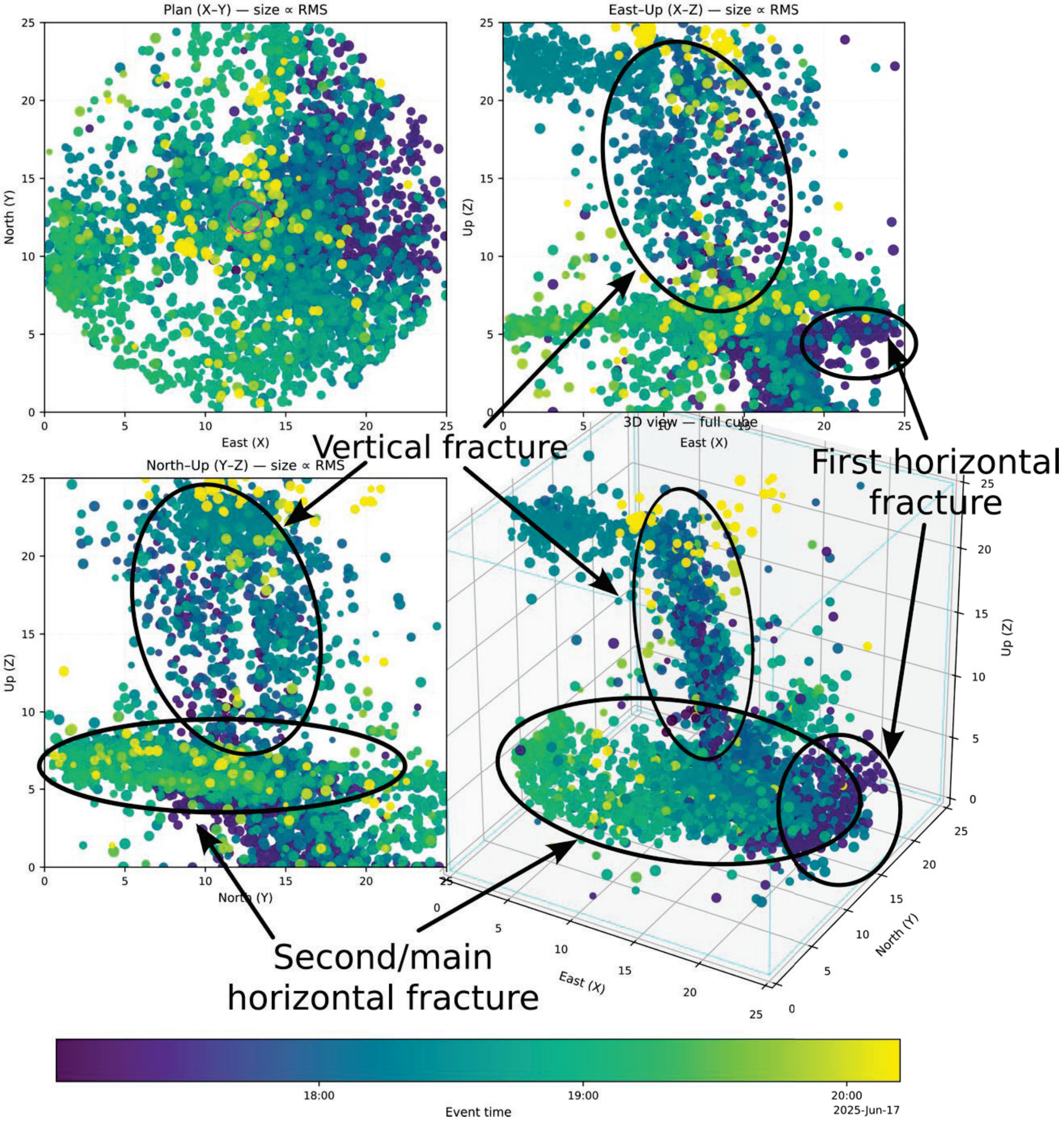

Figure 15. AE catalogue for injection sequence 2 showing early scattered clusters followed by a large, planar event cloud at the depth of the bottom notch. This planar cluster corresponds to the fracture propagated during this attempt. The other two clusters are not visible on the faces of the block and are believed to be very small fractures (not visible on the external surfaces nor within the wellbores).

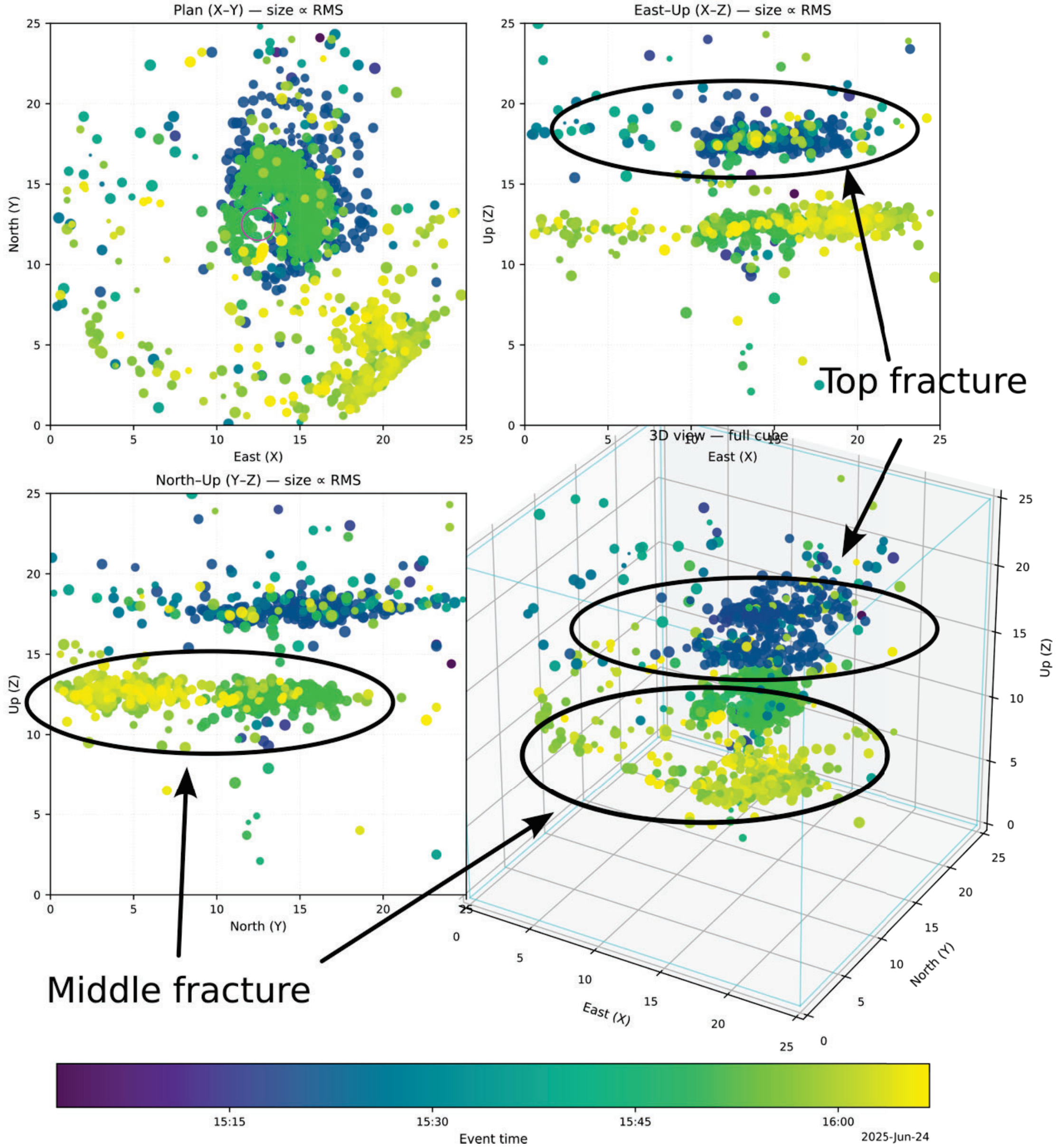

Figure 16. AE catalogue for sequence 3 exhibiting two compact event clusters at the levels of the top and middle notches, each corresponding to a successfully propagated fracture.

Overall, the AE-derived fractures matched with the surface traces observed on the external surfaces of the specimen. This was confirmed by fitting planes through the acoustic events and matching those planes with the position of the visible fractures on the faces of the sample. Figure 17 displays the acoustic event from the second and third injection along with the marking from the visible fractures on the block.

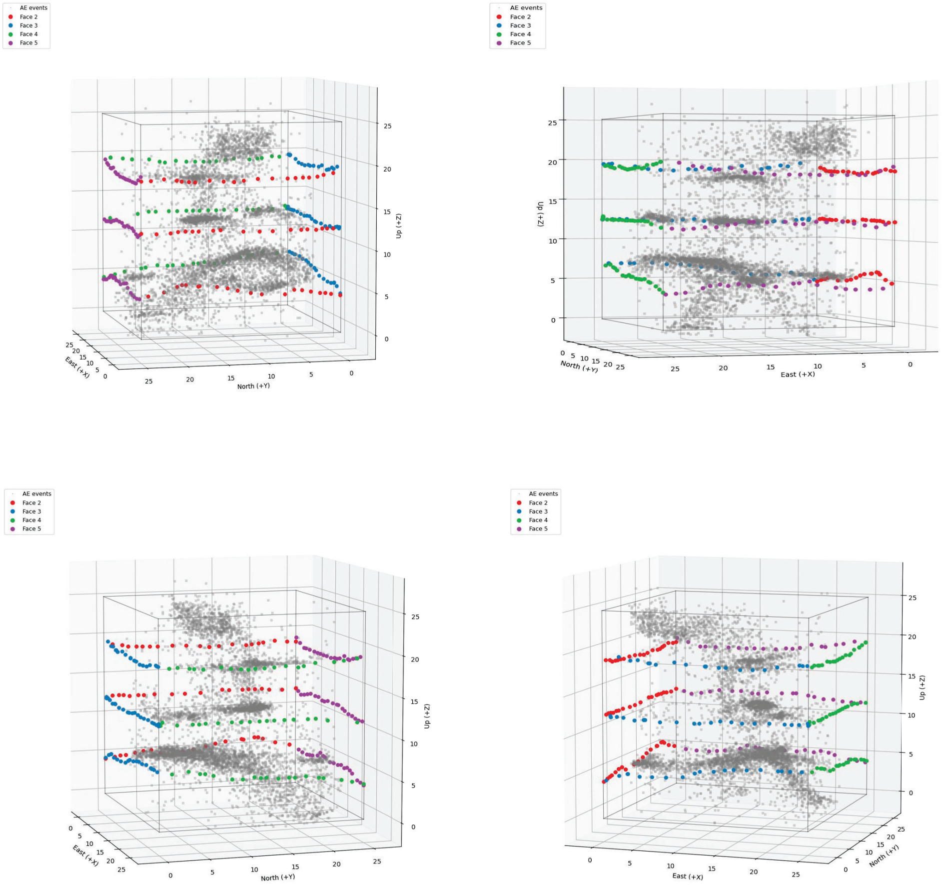

Figure 17. Superposition of the AE catalog of the second and third injections (in grey) with the 3 visible fractures on the outside of the sample.

For the second injection sequence, where active scans were acquired, P-wave transmissions were used to estimate fracture aperture. The results are shown in Figure 18 where the ‘acoustically’ estimated fracture opening using several source receiver pairs is plotted as a function of time. By matching the time of the apparition of the three fractures propagated during this attempt, one can see that they are visible in the opening calculations. Indeed, even if they are not normal to the propagation of the P-waves, the 3 structures clearly impacted the attenuation of the signal waves. These aperture estimates serve as geometric bounds; hydraulic transmissivity is presented in Section 2.1.7.

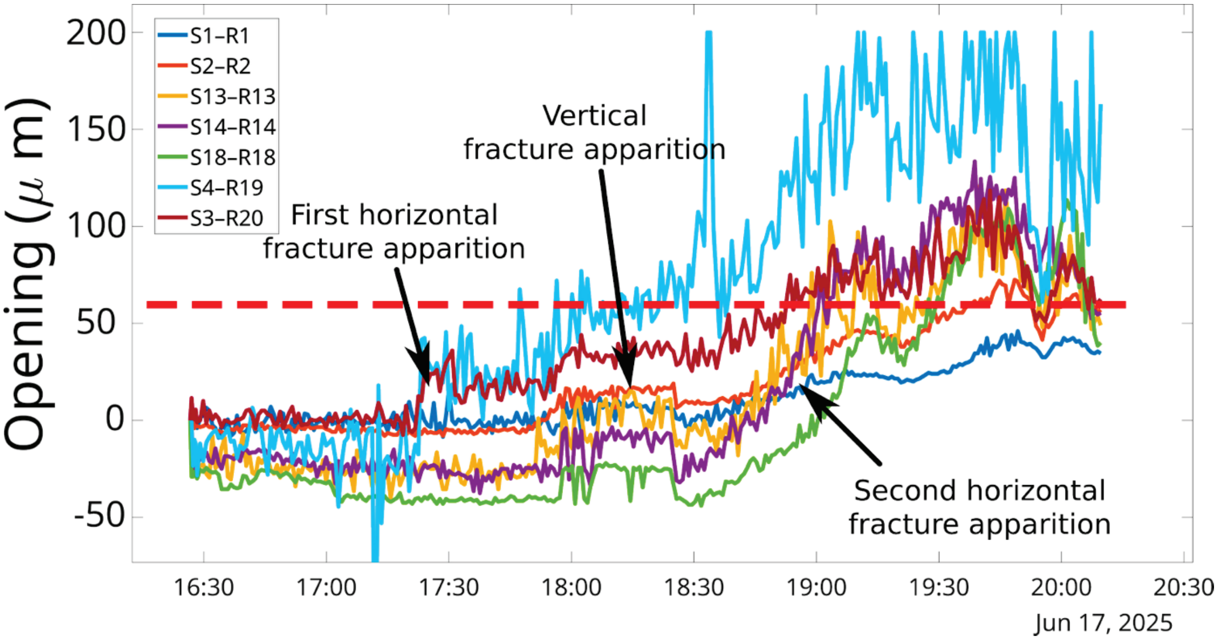

Figure 18. Estimated fracture apertures from P-wave transmission across the block during sequence #2. Step-like increases in apparent opening align with the propagation of the three observed fractures.

2.1.6 Fracture area estimation for 3 fracture sample

Although our fracture characterization mainly focuses on visible fracture geometry and AE activity we can still provide a simple estimate of the heat-transfer area of each fracture. Based on visual observations of the surface traces and the AE-inferred fracture planes, each fracture can be reasonably approximated as a horizontal planar surface cutting across our 25 cm × 25 cm block.

Under this assumption, a conservative lower-bound estimate of the fracture area is simply:

$A \approx 25\text{ cm} \times 25\text{ cm} = 625\text{ cm}^2$.

Since a fracture exposes two surfaces (upper and lower faces), the corresponding heat-transfer area becomes:

$A\text{Tot} \approx 2 \times 625\text{ cm}^2 = 1250\text{ cm}^2$ per fracture.

This estimate does not include any correction for roughness, aperture variations or irregular geometry, because these quantities cannot be directly measured with the available experimental tools. In reality, the effective area in contact with circulating fluid will be larger due to surface asperities, but this cannot be quantified here.

Even though the exact area cannot be measured, this does not limit our ability to analyse the energy exchanged between the fluid and the rock. The thermal evolution observed during the experiments is determined primarily by the measured temperatures and flow rates, and these directly reflect how much heat moves through the system. For this reason, a detailed or high-precision measurement of fracture surface area was not required for interpreting the laboratory results.

2.1.7 Fracture characterization

Once the completion was done, the different created fractures were characterised hydraulically by performing injection tests for all injection–production combinations at different injection flow-rates. Measured pressure stayed well below the pump limit (<1 MPa vs a 50 MPa limit), confirming a much higher permeability than previous samples. These injections reached steady-state sufficiently fast to allow an estimation of the fracture hydraulic transmissibility.

The hydraulic transmissibility submitted to a radial flow directly controls the well injection pressure at steady-state:

$$\Delta p = \frac{\mu Q}{2\pi T} \ln\left(\frac{r_0}{r_w}\right)$$

where T is the hydraulic transmissibility (in cubic meters) defined as the product of fracture permeability times fracture thickness, μ is the viscosity of the injected fluid, Q is the flowrate, ΔP is the pressure differential across the flow domain, r_0 is the radius at which the pressure is constant at atmospheric pressure (in our case the outlet wells) and r_w is the radius of the well. Fracture aperture estimates obtained from acoustic transmission (Section 2.1.6) provide geometric constraints on fracture opening. For flow and heat-transfer analysis we rely on the hydraulic transmissivity T, which inherently accounts for roughness of the surface, the presence of channels and aperture variation. We believe it is the appropriate parameter for interpreting the circulation experiments.

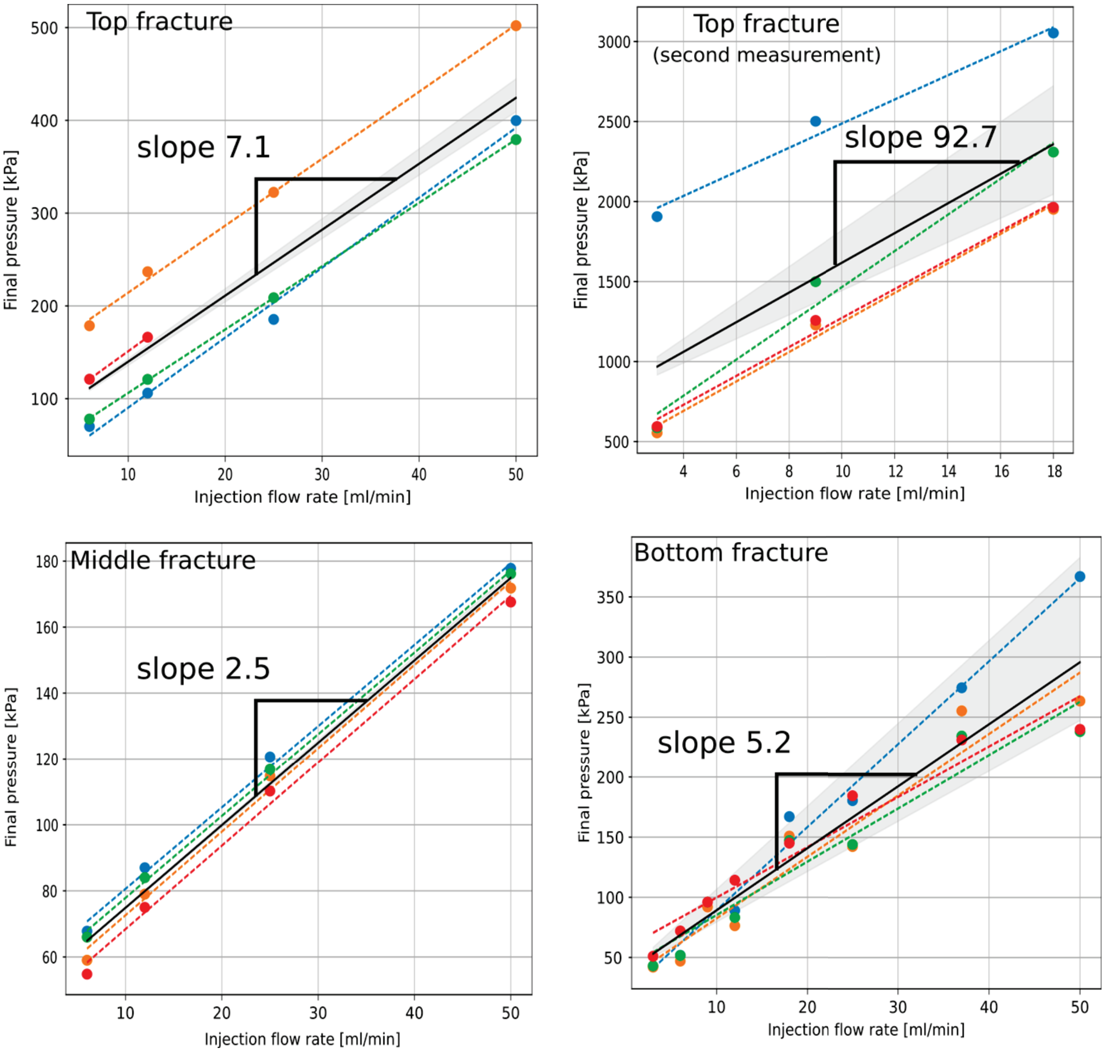

Figure 19. Steady-state injection pressure measured for all production wells in the three-fracture block. The resulting fracture transmissibility shows significant difference in the fracture hydraulic properties between the three fracture planes.

Figure 19 presents the measured pressure at steady-state as function of different imposed flow rates in the different fractures. For each fracture, injections at a different flowrate were made 4 times: Once with all the outlet wells open and three times with only one of the wells open. From those measurements, we can calculate the transmissibility of the fracture from the slope of the steady-state pressure as function of the injection rate.

Using the same radial-flow relation as for GABB-11, the slope of the ΔP–Q curve for the LANH-02 fracture gives a hydraulic transmissibility of order 10^{-17}. This is roughly two orders of magnitude smaller than the transmissivities measured for the GABB-11 fractures (Table 2), which is consistent with the much higher pressures required to sustain comparable flow rates in LANH-02.

To complement the transmissibility measurements, we also estimated an effective hydraulic aperture for each fracture. This is done using the classical cubic law, where for a Newtonian fluid flowing in a fracture of uniform aperture ω, the cubic law gives the fracture radial transmissibility:

$$T = \frac{w^3}{12}$$

where T is the fracture hydraulic transmissibility (in m^3).

We applied this relation to the transmissibility values measured for the three fractures. These estimated apertures are included in Table 2. Since the cubic law assumes smooth, parallel walls, these values should be interpreted as effective hydraulic apertures, not true geometric openings.

The estimated apertures fall in the range of ~10–35 μm, which is consistent with the order of magnitude obtained from the acoustic inversion for the bottom fracture displayed in Figure 18. However, it is important to note that the relevant measure with respect to FTES is the fracture transmissibility. Its estimation directly from flow measurements should be used.

Table 2. Hydraulic Transmissibility of the different fractures in GABB-11 and LANH-02

	Fracture transmissibility (m^3)	Estimated aperture from the cubic law (directly from transmissibility)	Estimated aperture (from active acoustics transmission)
Top fracture	1.1×10^{-15}	23.6 µm	No data
Top fracture (Second measurements)	8.7×10^{-17}	10.1 µm	No data
Middle fracture	3.2×10^{-15}	33.7 µm	No data
Bottom fracture	1.6×10^{-15}	26.8 µm	~50 µm
LANH-02	1.3×10^{-17}	5 µm	No data

Over the course of our experiments campaign, we noticed on several occasions that the transmissibility of certain fractures (namely the top one and the middle one) appeared to be changing drastically between experiments. Upon measuring it again (see Figure 19 and Table 2: Top fracture (second measurements)) we observed that it had decreased by a factor of 13. We believe that this apparent “closing” of the fracture is actually caused by an obstruction of our inlet and outlet wells by fines (small particles detached from the fracture surface). This clogging is still under investigation. As we are conducting our FTES experiment under an imposed flowrate, this is not of a major concern as we only observed higher injection pressures when clogging occurs. The injected water was flowing at the same rate, just at a higher pressure. It did cause the sealing on the faces of the cube to fail more often because of the higher stress imposed on them by the water in the fracture.

2.2 Drilling of additional wellbore and creation of a circulation loop

Once the fractures were created through our samples, we cored outlet wellbore(s) that intersected with the fracture(s). In the single fracture samples, a single outlet well was made for each. They were cored vertically in one of the corners of the top face of each block at 10 cm from the injection wellbore. The coring stopped when it reached the fracture, giving us valuable information about the exact position of the fracture in that area. Those wells were completed just above the fracture with a steel completion tool and epoxy. Figure 20 displays a schematic of the completion for single fracture samples.

In the three-fracture block, we wanted to have more outlet wells and to isolate them from the outlet of the other fractures. To do this, we used the same completion design for the outlet wells as for the injection completion tool (see Figure 10). However, instead of having them made from steel, we resorted to 3d printing the pieces. It allowed us to easily attach temperature sensors that were meant to measure the water temperature coming out of the fracture. Three outlet wells were cored vertically from the top face of the sample. They were arranged in a circle of 10.5 cm radius centered on the injection well. This configuration offered the largest distance between the inlet and outlet wells while keeping them all three at the same distance. Figure 20 (right) displays a schematic of the completion for the three-fracture sample.

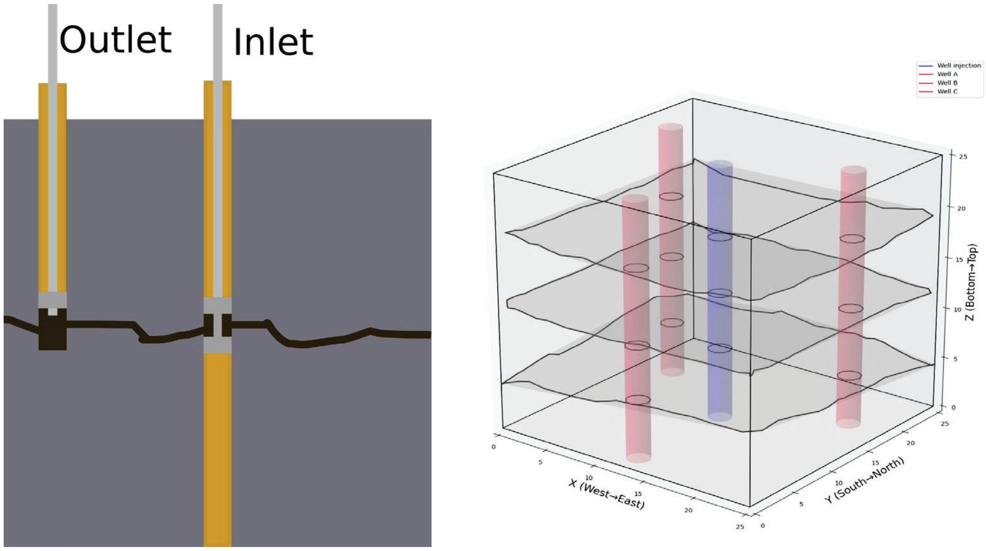

Figure 20. Schematics of the completion of the inlet and outlet wells in a single fracture sample. The yellow filling in each well is epoxy resin, while the dark grey items are the completion tool placed at the bottom of the outlet well and in the middle of the injection well. Right: 3D view of the distribution of the outlet wells (in red) in the three-fracture sample.

In summary, with one central injection well and three outlet wells, each of them completed with three distinct lines for each fractures, we have a versatile system with a lot of flexibilities in terms of injection/circulation protocol.

2.2.1 Sealing of the fractures (on the outside of the samples)

The fracture(s) intersection with the external faces of the samples were sealed up by using a mix of epoxy and glass fiber to create a closed system where water would only flow out through the designated outlets. In all cases, the sealing eventually leaked, especially when subjected to high pressure over extended periods of time. We therefore removed and reapplied the mix of epoxy and glass fiber when required.

2.2.1.1 Injection heating system

Two approaches were implemented to heat the injection fluid before its entrance into the specimen, with the requirement to be able to inject at a constant temperature. The initial system consisted of an oil bath, in which the stainless-steel injection tubing was immersed (Figure 21). While functional, this setup required constant manual adjustment of the hot plate to maintain a stable temperature and presented safety concerns due to the exposed heated oil. It was therefore abandoned after few tests.

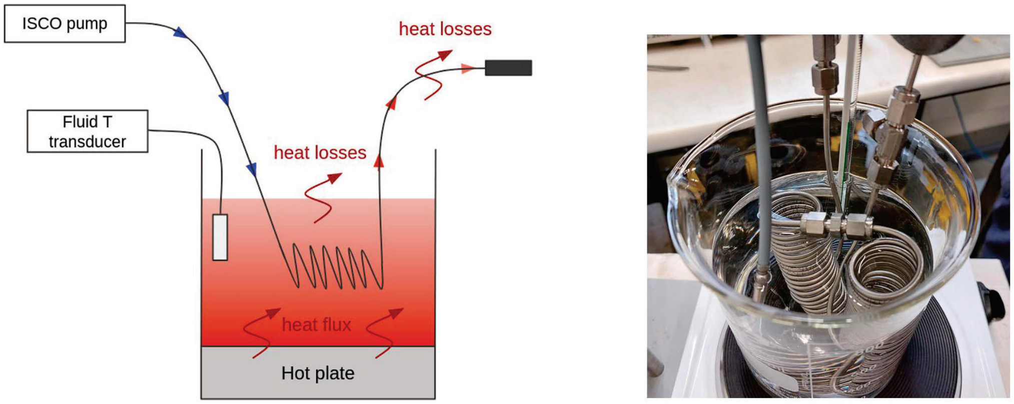

(a) Schematic representation of the heating system setup

(b) Photograph of the experimental setup

Figure 21. Initial heating system based on immersing the injection tubing in a temperature-controlled oil bath. Although effective, this setup required constant manual adjustment and presented safety concerns due to exposed hot oil.

The final system used resistive heating tapes wrapped around a long section of stainless-steel tubing and regulated by a PID controller (Figure 22). The PID feedback relied on a thermocouple sensor (M12JSS-(M6)-U-200-A from RoHS) installed in the circuit. The placement of this control sensor was progressively improved during successive experimental cycles. Initially attached to the outside of the steel tubing, it overestimated the fluid temperature and responded slowly due to the thermal inertia of the metal. When later positioned inside the tubing, but slightly outside of the main flow, it underestimated the true inlet temperature at low flow rates. After further adjustment, the sensor was installed at the center of the flow path, allowing accurate measurement of the fluid temperature entering the sample.

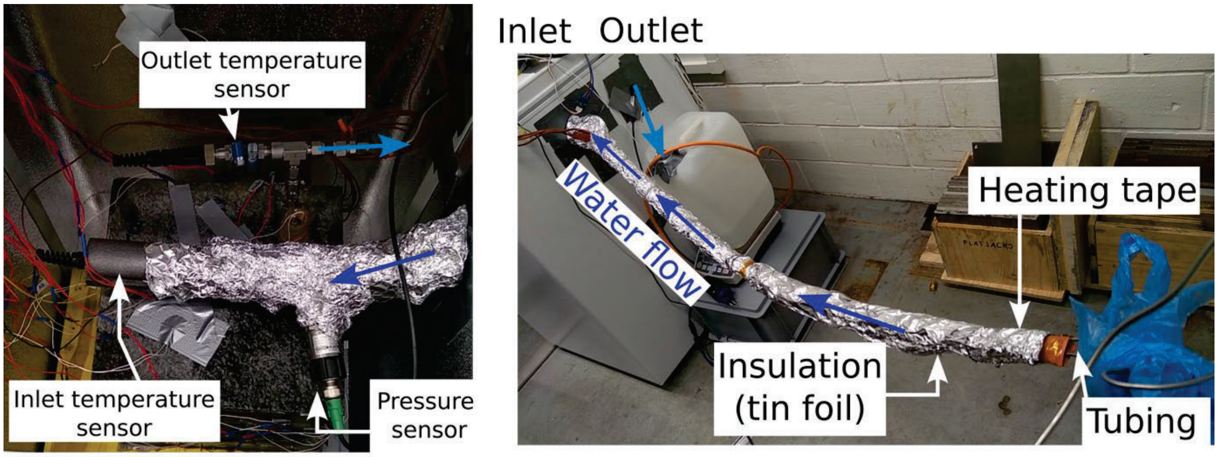

Figure 22. Heating tape system to heat the injection water at a constant temperature. In this system the water flows through a metal tube with heating tape wrapped around it. The heating tape power supply is controlled by a PID controller (feedback controller) that monitor the water temperature at the inlet of the sample. It adjusts the heating to automatically maintain the injected fluid temperature constant.

For safety, an additional thermistor monitored the temperature of the tubing near the inlet. If the tubing temperature exceeded a predefined threshold (for example is the pump stopped by mistake) the safety circuit automatically shut down the heating power to prevent overheating. Since heating occurred while the fluid transits through the tubing, the maximum achievable inlet temperature depended on the injection flow rate. Performance was enhanced by thermally insulating the tubing with aluminum foil and by routing the tube back and forth along the heating tape to increase the effective heating length. The achievable inlet temperatures for different flow rates are summarized in Table 3.

Table 3. Achievable inlet fluid temperatures (for injected water) as function of the injection flowrate with the PID-controlled heating tape system

Injection flowrate	Maximum achievable temperature
1 mL/min	150°C
10 mL/min	150°C
25 mL/min	80°C
50 mL/min	50°C

A typical FTES experimental sequence consisted of a heating phase, where hot water was injected through the central well and cooled water was collected from the peripheral wells, followed by a pause without flow. The following cooling phase involved injecting room temperature water through the same central well while recovering the heated water at the periphery.

2.2.2 Temperature monitoring of fluid and sample's surface

We monitored temperatures at three locations to characterize thermal loading and recovery:

- Fluid inlet temperature with a type-J thermocouple (M12JSS-M6-U-200-A from RoHS).

- Fluid outlet temperature at the bottom of each production well (SMT Ring Terminal Probe ETP-RT-4-20- 10K3A1B from VARIOHM) for the three-fracture setup and type-J thermocouple for the one fracture samples.

- Rock surface temperature with an array of thermistor sensors distributed on the faces.

The position of these sensors is displayed in Figure 23 and Figure 24. Pumps and heaters were automated in LabVIEW, while temperature logging was handled by Arduino MEGA boards.

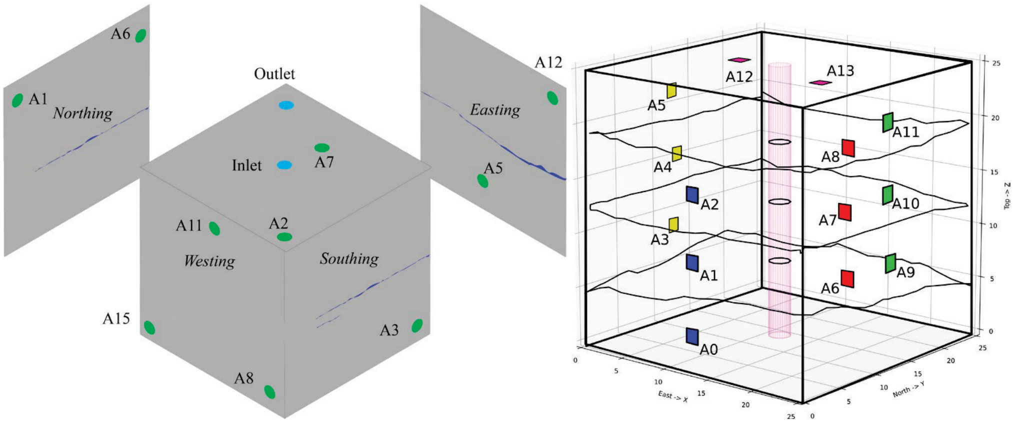

Figure 23. Detailed sketch with location of all surface temperature measurements. Left: GABB-08 sample. Right: GABB-11 sample.

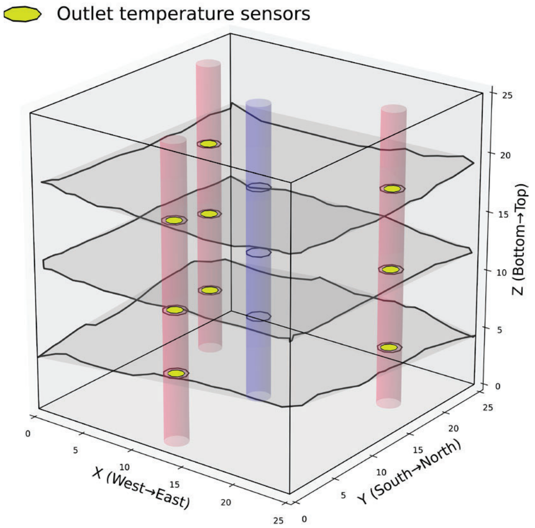

Figure 24. Outlet temperature sensor position for the three-fracture sample.

2.3 Laboratory thermal circulation

2.3.1 Single fracture samples

2.3.1.1 GABB-08 sample

Following fracture creation, a long charge–discharge sequence was done on the sample. Injection used the heating-tape loop (see Section 2.2.1.1) and proceeded at a constant rate of 0.3 mL/min. The protocol comprised 15 h of hot injection at 80 °C, followed by a 7 h pause, then 15 h of cold injection, and finally a pause. The inlet temperature was monitored and remained stable over the long windows of steady operation. In this experiment, the output well was only closed off at the top by a rubber plug, creating a large water reservoir in the outlet well. The low transmissibility caused the experiments to be performed at a high pressure inside the fracture. This caused the sealing of the fracture (fiber glass and epoxy) to leak multiple times. Figure 25 displays the temperature measurements made during a typical loading/unloading cycle performed on the GABB-08 sample.

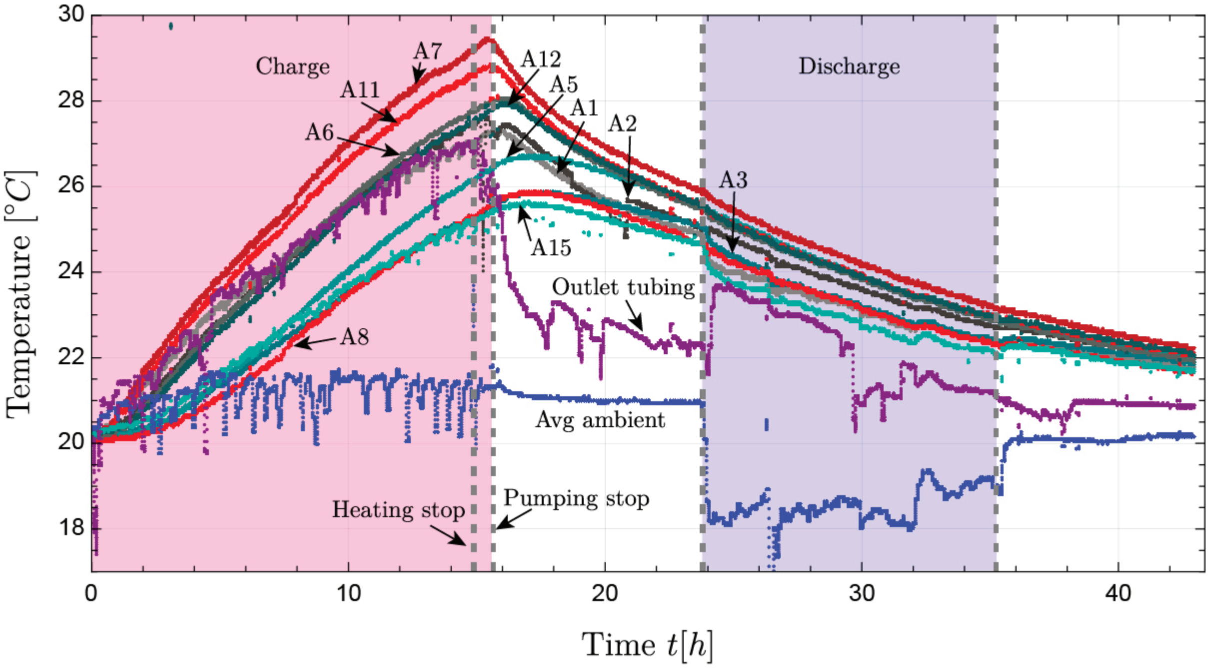

Figure 25. Thermal loading schedule and temperature recording for GABB-08.

2.3.1.2 LANH-02 sample

For this sample, thermal storage tests were done inside a turned-off freezer to reduce room-temperature fluctuations and drafts. This setup was not maintained for other experiments because it made it very difficult to access the sample. The heating loop was the tape-based system described in Section 2.2.1.1. Thanks to the higher permeability of this sample, we were able to explore multiple rate–temperature combinations covering 1, 2.5 and 5 mL/min and 75–150 °C. Experiment cycles were composed of 3 hours of hot water injections, 1.5 hour of pause during which no injection happened, 3 hours of room temperature (20 °C) injection and 1.5 hour of pause. In one campaign we achieved three full cycles before stopping due to a pump automation malfunction. All temperature sensors were present from the start: inlet thermocouple at the injection line, a thermistor at the bottom of the production well, and a surface array of thermistors on the faces. The data from the temperature sensors for a typical experiment (injection at 5 mL/min with water heated to 80 °C) is displayed in Figure 26.

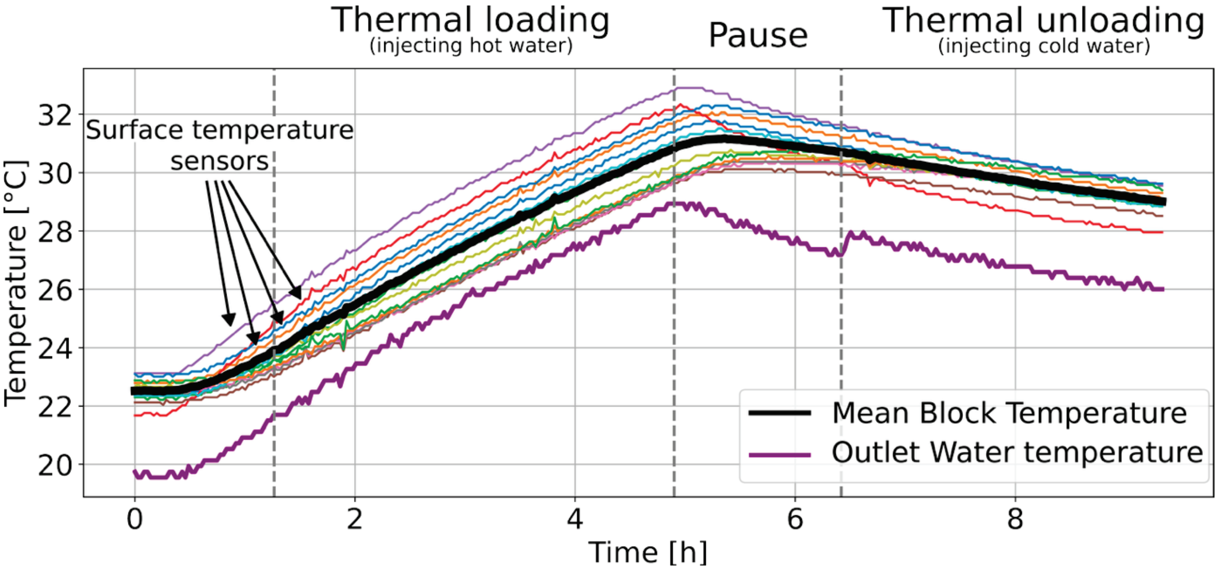

Figure 26. Thermal loading schedule and temperature recording for LANH-02

Using the LANH-02 sample, we also performed repeated cycles where the heating and cooling phase were repeated at regular intervals. Those results are discussed in Section 5.7.6.

2.3.2 Three fracture samples

2.3.2.1 GABB-11

The injection parameters that were applied remained almost identical between experiments done on this sample. The temperature was kept around 78 °C and the injection rate was either 25 or 5 mL·min⁻¹. The exact temperature was set due to heat loss along the injection line, preventing us from going hotter. Inlet temperatures were measured by thermocouples; each of the nine outlets had a thermistor; and the surface was instrumented with a dense thermistor array to resolve anisotropic heat spreading. The valve placed before each injection line allowed straightforward switching between three- and single-fracture configurations.

Early tests used 6 h hot / 3 h pause / 6 h cold / 3 h pause and 6 h hot / 6 h cold cycles. The emergence of a temperature plateau motivated longer 12 h hot / 1 h pause / 12 h cold cycles. Initially the sample allowed us to operate at low hydraulic pressure thanks to its high transmissibility. However, after a few cycles of experiments, the permeability of certain fracture appeared to greatly decrease as discussed in Section 2.1.6. The main hypothesis is that the outlet path through the wells has been on occasion blocked by debris from the fracture’s faces.

Table 4. Summary of laboratory thermal circulation experiments

Experiment label	Sample	Fracture	Injection rate	Injection temperature	Cycle duration (heating/pause/cooling/pause)
gabb08	GABB-08	/	0.3 mL/min	80°C	15h/7h/15h/7h
lanh-5-75	LANH-02	/	5mL/min	75°C	3h/1h30/3h/1h30
lanh-5-150	LANH-02	/	5mL/min	150°C	3h/1h30/3h/1h30
lanh-2.5-150	LANH-02	/	2.5mL/min	150°C	3h/1h30/3h/1h30
lanh-cycle_2	LANH-02	/	5mL/min	80°C	[3h/1h30/3h/1h30] x 2
lanh-cycle_9	LANH-02	/	5mL/min	80°C	[3h/1h30/3h/1h30] x 9
gabb11-25-3f	GABB-11	All 3	25mL/min	78°C	12h/1h/12h/1h
gabb11-25-M	GABB-11	Middle	25mL/min	78°C	12h/1h/12h/1h
gabb11-25-B	GABB-11	Bottom	25mL/min	78°C	12h/1h/12h/1h
gabb11-5-3f	GABB-11	All 3	5mL/min	78°C	12h/1h/12h/1h
Gabb11-5-T	GABB-11	Top	5mL/min	78°C	12h/1h/12h/1h
Gabb11-5-B	GABB-11	Bottom	5mL/min	78°C	12h/1h/12h/1h

2.3.3 Laboratory thermal test results and discussions

2.3.3.1 Inlet and outlet wells contribution to heat exchange

Despite being insulated by epoxy, the injection and production wells play a significant role in the thermal evolution of the block. Their surface area is small compared with that of the fractures (2%), yet they present the largest temperature contrast with the surrounding rock. As a result, they tend to exchange heat with the block, especially the injection well.

In all experiments, the surface temperature measurements showed a clear asymmetry between the upper and lower halves of the block, with higher temperatures observed above the fracture during heating. This anisotropy persisted throughout the hot injection phases and even during the temperature plateau (observed for long experiments), indicating that the wells contribute continuously to the redistribution of heat within the sample. During cooling, the situation was reversed: the top part of the block cooled more rapidly than the lower half, consistent with the wells having strong capacity to exchange heat because of the higher temperature difference.

This effect is illustrated in Figure 27, which displays the evolution of the average block surface temperature and the evolution of the temperature of the upper and lower regions for two representative experiments (performed on LANH-02 and GABB-11). The temperature difference between the two sub-sections of the block does not vanish during steady-state operation, confirming that the wells influence the spatial distribution of heat in our samples. These local exchanges should be much smaller in large-scale field systems, where the ratio between the wells and fractures areas is much smaller. However, it must be taken into account when interpreting our laboratory results and should be included in any numerical modelling of these experiments.

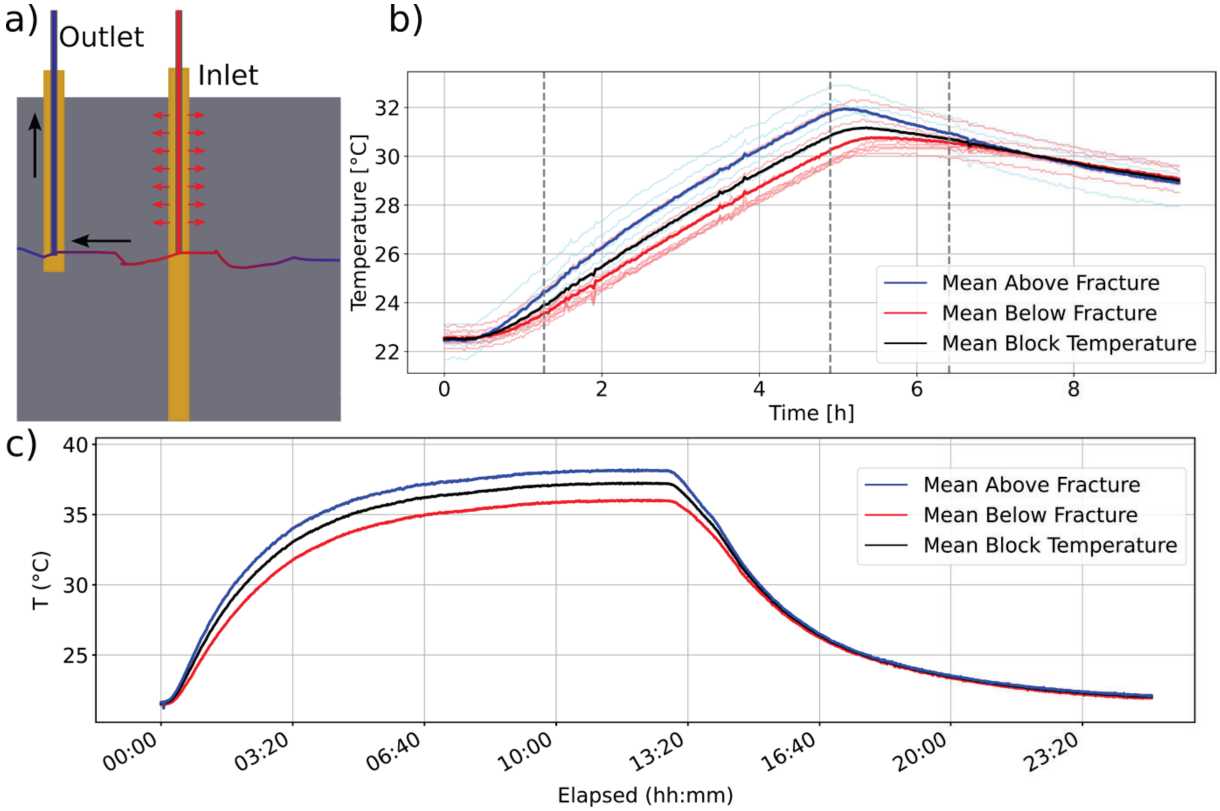

Figure 27. Evolution of the average block surface temperature and of the temperatures measured on the upper and lower halves of the block for two representative experiments (LANH-02 and GABB-11). The persistent temperature difference between the two regions during heating, plateau, and cooling phases illustrates the significant contribution of the injection and production wells to internal heat exchange.

2.3.3.2 Effect of injection rate on heating rate of the block

The injection rate controls the rate at which thermal energy is supplied to the fracture network. For a given injection temperature, a higher flow rate corresponds to a larger injected thermal power and therefore a faster heating of the rock volume. Figure 28 illustrates this effect for LANH-02, where 2 experiments were performed at 2 different injection rates with the same inlet temperature (150C).

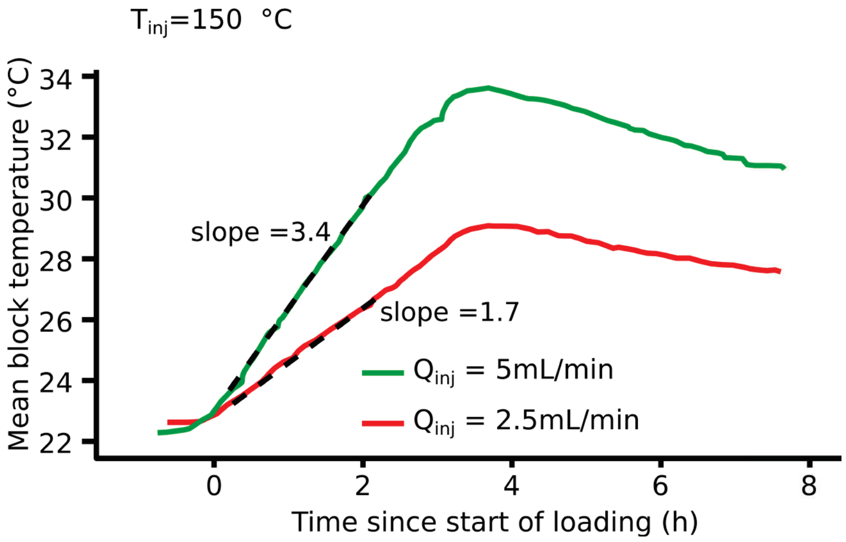

Figure 28. Average surface temperature of LANH-02 during thermal injections at two flow rates (5 and 10 mL/min). The early-time heating is approximately linear, and the heating rate increases with flow rate, consistent with a scaling proportional to the injected thermal power.

During the early phase of heating, the increase in the average surface temperature of the block is approximately linear in time. The slope of this linear increase scales proportionally with the injection rate, confirming that the heating rate is directly controlled by the injected thermal power. At later times, the heating curves progressively approach a plateau that reflects the balance between injected power and heat losses (mainly radiation and external convection), but the initial heating phase remains largely governed by advection of hot water within the fracture.

These observations are consistent with the conceptual view that, under advection-dominated conditions, the injection rate primarily determines how quickly thermal energy is delivered to the system, while the eventual equilibrium temperature is set by boundary losses and the thermal diffusivity of the surrounding rock.

2.3.3.3 Effect of block temperature on injection pressure

Thermal effects also influence the hydraulic behaviour of the system. Figure 29 shows three thermal injection experiments performed on the LANH-02 sample at the same flow rate of 5 mL/min but at three different injection temperatures of 75, 80 and 150 °C. Two key features can be observed.

First, the experiment with the highest injection temperature systematically exhibits the highest injection pressure. Second, within each individual experiment, the injection pressure increases progressively during heating as the block warms up. Since the flow rate is constant, this increase in pressure reflects a reduction of the effective hydraulic transmissivity of the fracture during heating.

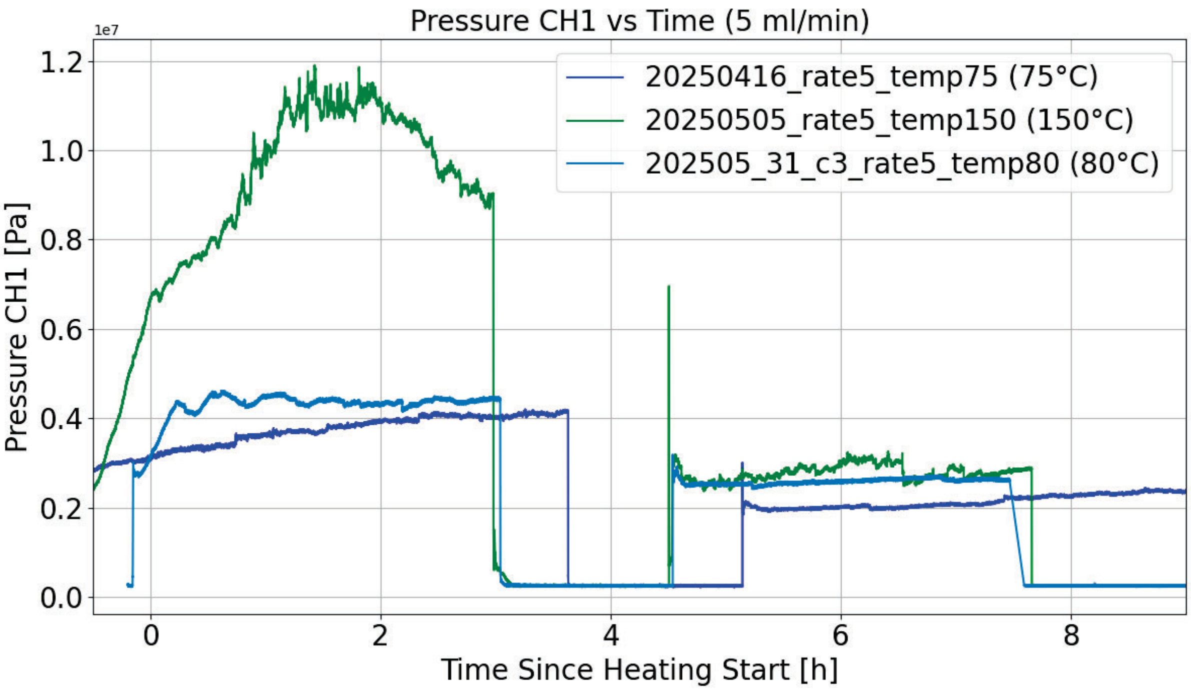

Figure 29. Injection pressure and block temperature for LANH-02 at a fixed flow rate (5 mL/min) and three inlet temperatures. Higher inlet temperatures yield higher injection pressures, and pressure increases during heating within each experiment, consistent with a reduction in transmissivity as the block warms.

We interpret this behavior as the result of the thermo-elastic response of the rock. As the block heats up, thermal expansion reduces the aperture of the fracture, which in turn increases the pressure required to maintain the same flow rate. This effect is clearest in low-transmissibility samples such as LANH-02, where small changes in aperture translate into measurable differences in hydraulic resistance. In the present study, the behavior was not always reproducible across samples, but it is consistent with similar observations made during decameter-scale thermal injection tests conducted by PNNL and SNL. The possible coupling between thermal loading and fracture transmissivity is therefore an important topic for future investigation.

These results illustrate that the hydraulic behavior of a fracture during thermal injection is sensitive to temperature. Understanding this thermo-hydraulic coupling will be important for evaluating long-term FTES behavior under repeated charge–discharge cycles.

2.3.3.4 Strong advection regime

Our experiments allowed us to observe two distinct regimes of operation. In the high-power, high-transmissivity configurations (ex: GABB-11, fractures with high transmissivity, operated at 25 mL/min and 78 °C or LANH-02 operated at 5 mL/min and 150 °C), the outlet temperature exceeds the average block temperature: the injected water does not have time to transfer all of its heat to the rock, and a significant fraction of the energy is advected out of the system. In contrast, in lower-power or lower-transmissivity configurations (e.g. GABB-08, and GABB-11 operated at 5 mL·min^{-1} and 80 and 78 °C), the outlet temperature remains below or close to the block temperature, indicating that most of the injected heat is transferred to the rock before the water exits the sample.

Those two different regimes are illustrated in Figure 30.

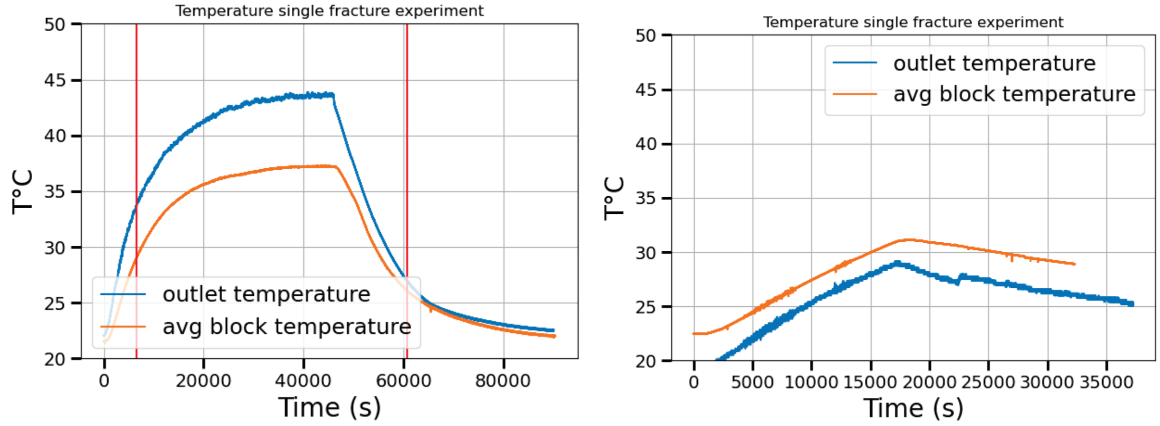

Figure 30. Evolution of the outlet water temperature and the average block temperature for the 2 different regimes. Left: High injection power/ high advection regime (injection rate 25 mL/min, injection temperature 78 degrees). Right: Low injection power regime (injection rate: 5 mL/min, injection temperature 80 degrees).

To make the distinction between the two regimes more explicit, Table 5 summarizes, for a few representative experiments, the fracture transmissivity (where available), the imposed flow rate, and the corresponding fracture Peclet number. The Peclet number is defined as:

$$\mathrm{Pe}_f = \frac{uL}{\alpha_r}$$

where u is a characteristic fluid velocity along the fracture, L the injection–outlet distance (≈ 0.10–0.15 m), and α_r the thermal diffusivity of the rock. In practice, we estimate u from the imposed flow rate and the effective fracture aperture inferred from the cubic law (Section 3.2.4), and we take $\alpha_r \approx 10^{-6} \mathrm{m}^2/\mathrm{s}$, a typical value for crystalline rocks.

The Peclet number allows us to classify each experiment into a high-power, advection-dominated regime or a lower-power, more storage-efficient regime. This is shown in Table 5.

Table 5. Hydraulic transmissibility, estimated aperture, injected flowrate, injected temperature, Peclet number and associated regime for a selection of experiments.

Experiment	T (m^3)	ω (µm)	Q (mL/min)	T_{inj} (°C)	Pe_f	Regime
gabb08	Very low		0.3	80		Low injected power Pe_f<1000 $T_{outlet} < T_{inlet}$
lanh-5-75	1.3×10^{-17}	5	5	75	6×10^2	
gabb11-5-B	1.6×10^{-15}	26	5	78	5×10^2	
gabb11-5-T	1.1×10^{-15}	22	5	78	6×10^2	
lanh-5-150	1.3×10^{-17}	5	5	150	6.5×10^3	High injected power

gabb11-25-M	$3.2x10^{-15}$	34	25	78	$3x10^{3}$	$Pe_f>1000$ $T_{outlet}> T_{inlet}$
gabb11-25-3f	$3.2x10^{-15}$ (dominated by middle fracture)		25	78	$3x10^{3}$	

Overall, these two regimes reflect a balance between the residence time of the circulating fluid and the rate at which heat can diffuse into the rock. When the flow rate or injected temperature are high, the residence time becomes too short and part of the injected energy is simply carried out of the system, resulting in a less efficient storage configuration. In contrast, experiments operated at lower flow rates (like the 5 mL/min tests at 78 °C) sit closer to the transition between the two regimes, where the outlet and block temperatures converge and most of the injected heat is effectively absorbed by the sample. For future FTES efficiency measurements, operating conditions in this lower-power range are therefore preferable, as they maximise the fraction of energy actually transferred and retained by the rock.

2.3.3.5 Experimental Plateau Behavior of the Surface Temperatures

During long heating phases, the surface temperature of the blocks systematically follows three successive sub-phases. This behaviour is particularly clear in the long-duration experiments conducted on sample GABB-11 and are illustrated in Fig 5.5.

In the first sub-phase (Fig 5.5.b), immediately after the start of hot water injection, the surface temperature remains essentially unchanged. The hot fluid is confined to the vicinity of the injection well and the connected fracture, and the thermal front has not yet reached the external faces of the specimen. Heat is mainly transported **along** the fracture plane and starts to diffuse into the surrounding rock, but this effect is still localised and not resolved by the surface thermistors. The duration of this early phase depends on the transmissivity of the fracture, the injection rate and the size of the block, which together control the propagation speed of the thermal front.

The second sub-phase (Fig 5.5.c) begins once the thermal front reaches the external surfaces of the block. From this point onward, the mean surface temperature increases almost linearly with time. This regime corresponds to conduction-dominated heat transfer from the fracture plane toward the outer faces. The slope of this linear increase defines an effective heating rate of the block and is used later in the comparison between different injection configurations and flow rates. The duration of this phase and the value of the heating slope are controlled by the thermal diffusivity of the rock and by the imposed temperature difference between the injected water and the initial block temperature.

The third subphase corresponds to the later-time plateau behaviour. After the initial transient and the linear increase, both the outlet water temperature and the average surface temperature tend toward a quasi-steady value and vary only slowly over several hours. This is illustrated in Figure 31 for experiment GABB11-25-M, where a clear plateau is observed in both the block surface temperature and the outlet temperature.

This plateau results from the competition between:

- the heat input from the injected hot water

- the heat lost from the outer surfaces of the block to the surroundings.

Once these two effects balance each other, the surface temperature reaches a quasi-steady value, and the system approaches an approximate thermal steady state.
At this stage:

- the outlet temperature becomes nearly constant,
- the mean surface temperature on each face evolves very slowly,
- and the overall retained energy increases only marginally.

This plateau will be useful for the calibration of the heat loss coefficient used later in Section 5.7.3.

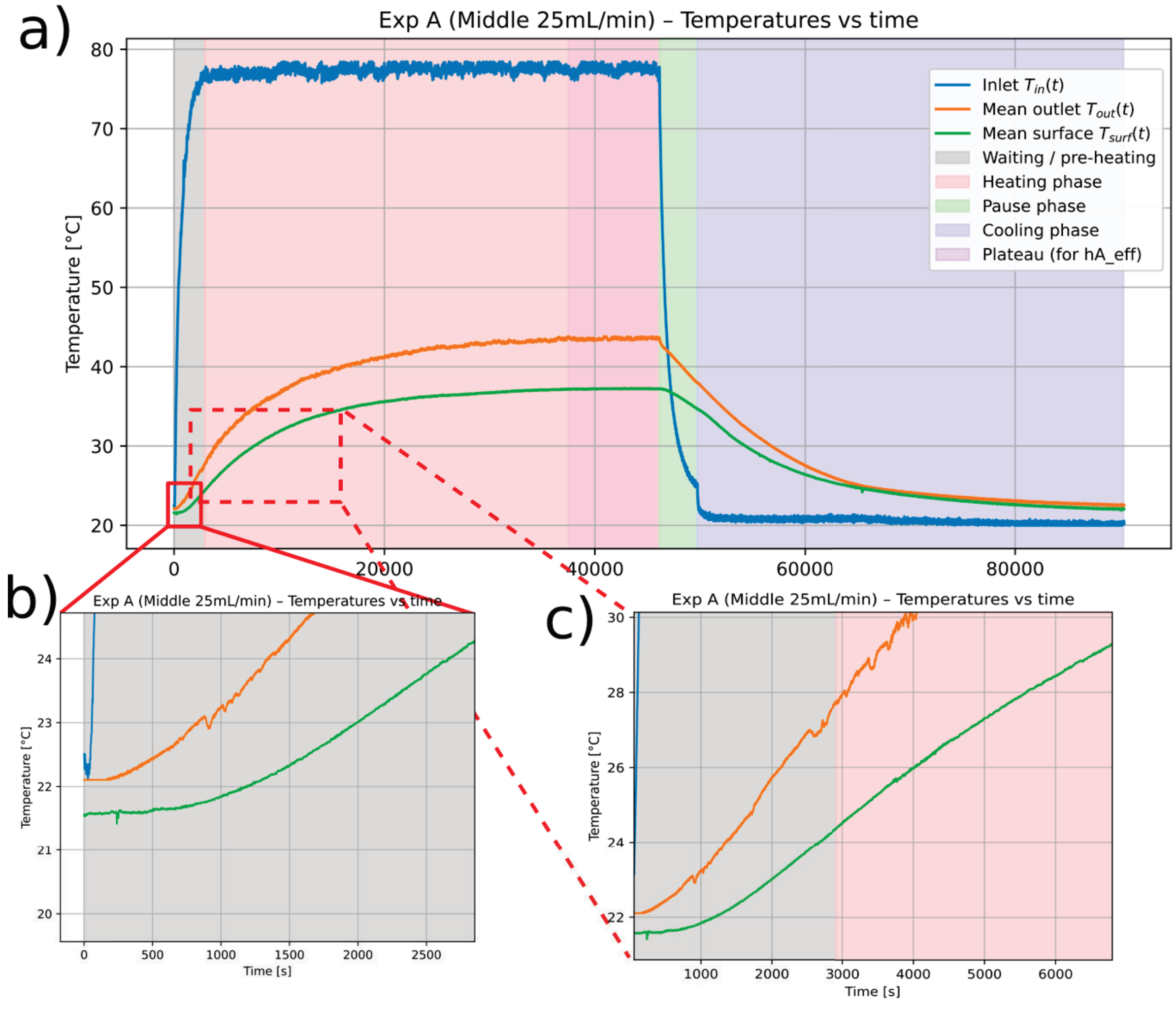

Figure 31. Evolution of the recorded data for experiment gabb11-25-M performed on the GABB-11 sample with a single fracture open (middle one), injection rate of 25 mL/min and

injection temperature of 78 degrees. We can clearly see a plateau in both block surface temperature and outlet temperature.

2.3.3.6 Multiple fractures effect on block heating

Experiments were performed both with a single active fracture and with all three fractures open simultaneously. At first glance, the overall/global thermal response of the block was almost identical in both configurations. The average temperature of all surface-mounted sensors on the sample presented in Figure 32 increased at the same rate and reached the same plateau, despite the larger exchange surface provided by the additional fractures. Here the plateau is defined by the part of the curve once the block temperature has reached 95 % of its maximum value. The heating slope, plateau arrival times and plateau temperature are displayed in Table 6.

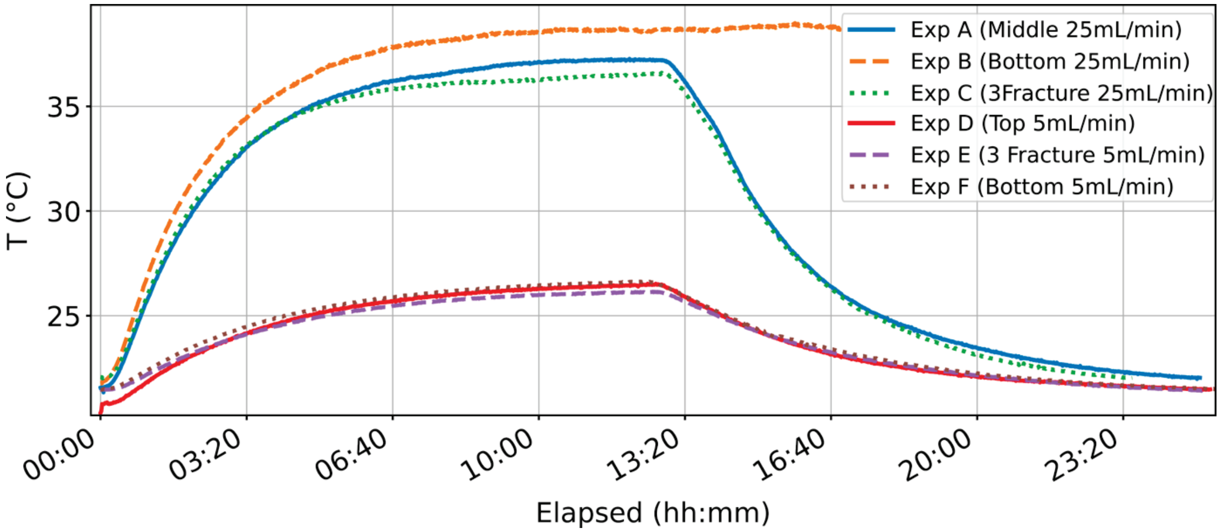

Figure 32. External mean block temperature measured during heating experiments on sample GABB-11, comparing single-fracture and three-fracture configurations at various injection flow rates. Despite larger exchange surface in multi-fracture tests, the overall heating response and plateau temperature are nearly identical.

Table 6. Heating slope, plateau arrival times and plateau temperature for various experiments performed on the GABB-11 sample.

Experiments	Heating slope (1st hour) (°C/min)	Plateau time	Plateau temperature
A (gabb11-25-Middle)	8.4 10^{-2}	5h55	41 °C
B (gabb11-25-Bottom)	9.5 10^{-2}	No data	43 °C
C (gabb11-25-3fracture)	8.3 10^{-2}	4h59	40 °C
D (gabb11-5-Top)	2.3 10^{-2}	6h06	26 °C
E (gabb11-5-3fracture)	1.7 10^{-2}	5h51	26 °C

F (gabb11-5-Bottom)	1.9 10^{-2}	5h59	27 °C

This data shows that, with the injection parameters that we have tested so far, increasing the number of active fractures did not improve the system's ability to store energy and we had no impact on the plateau and the mean heating rate. This holds both for cases where the outlet temperature exceeded the block temperature (strong advective contribution) and for cases where $T_{out} \approx T_{block}$: in both situations, the average block temperature evolution remained the same between experiments with one or three fractures.

2.3.3.7 Spatial temperature distribution

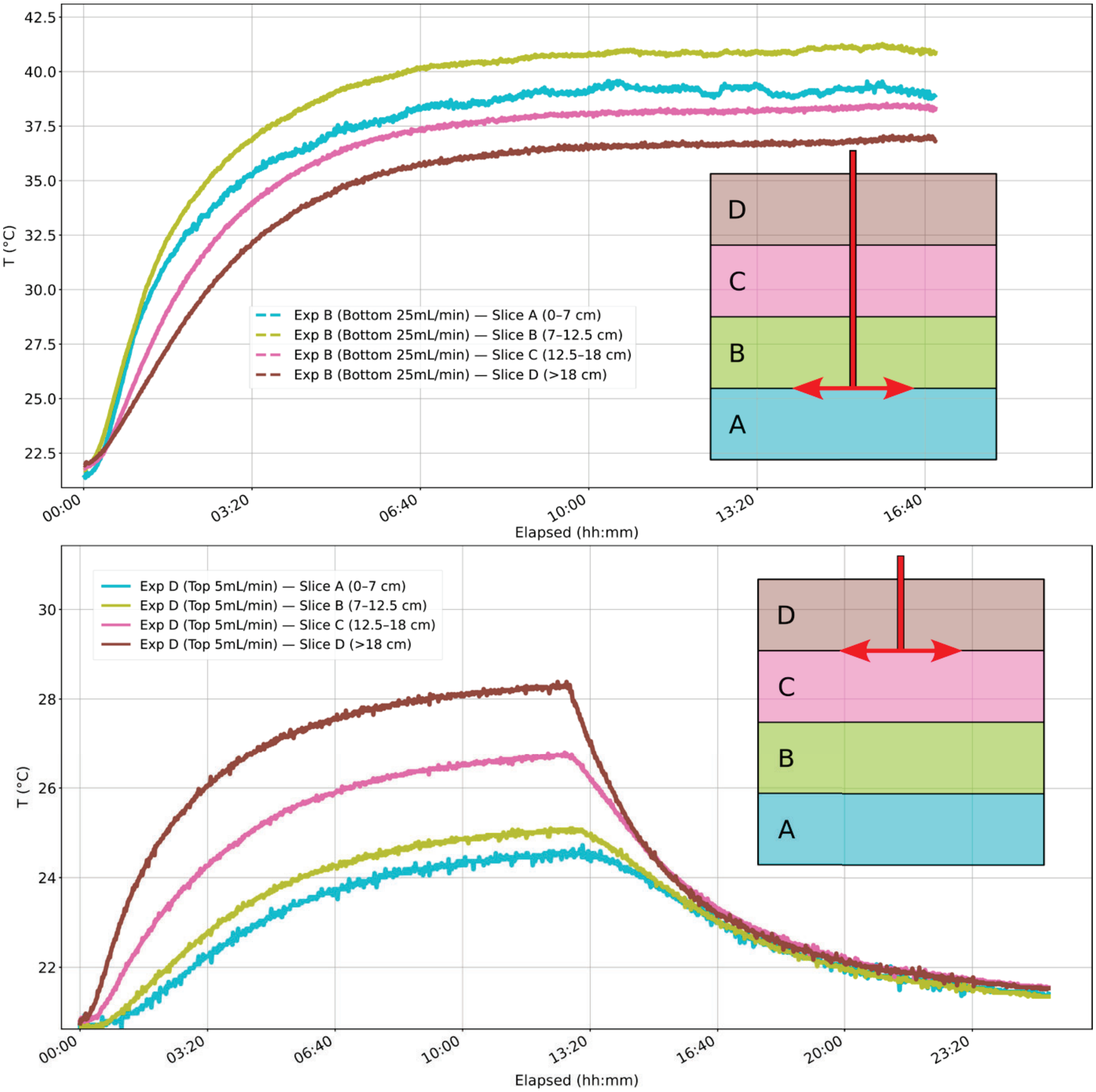

Figure 33. Spatial distribution of temperature within the GABB-11 block during heating, shown for four slices (A to D, from bottom to top) separated by the fracture planes. The temperature evolution clearly shows that heat

However, the spatial distribution of temperature shows that the heat does originate from the fracture where the injection takes place. This is displayed in Figure 33 where we plot the temperature of the block for different “slice” of block (section of the block separated by fractures). We define 4 slices A, B, C and D going from bottom to top. The heat propagated from this fracture into the block, confirming that each fracture acts as an independent exchange surface. Even if the overall response of the block appears similar for one or three active fractures, the distribution of temperature within the rock clearly reflects which fracture was used for injection.

These observations tell us that, the system-level response of our experimental setup in the explored injection parameters is mainly governed by the external losses and finite volume rather than by the number of active fractures.

2.3.4 Thermal Recovery Factor of the laboratory FTES

The FTES system investigated in the laboratory is a finite-size prototype. Its dimensions, thermal boundary conditions and heat-loss mechanisms differ from those of a field-scale reservoir embedded in a continuous rock mass. In particular, the created fractures span the whole specimen which exchange (loose) thermal energy with its surroundings. Because of this, the thermal behavior measured during the experiments can be divided into two parts. Some features are intrinsic to fractured thermal energy storage, such as the exchange of heat between the circulating fluid, the hydraulic fractures and the surrounding rock. Other features, however, arise entirely from the laboratory configuration itself. The block is small, its faces are exposed to ambient air, and heat leaks continuously from the sample to the room through radiation and natural convection.

To interpret laboratory results correctly, it is therefore necessary to construct a global energy budget. The aim is to follow how thermal energy moves from the fluid into the rock, how much of it is stored, how much is eventually recovered, and how much is lost to the environment. We consider the system as two coupled domains: the fluid-saturated domain, consisting of the wells and the fractures, and the rock domain, consisting of the solid block itself.

For clarity we introduce the following naming convention for the main energy and power quantities:

- Injected thermal power P_{inj} , and its time-integrated energy injected energy E_{inj}.
- Produced (outlet) thermal power P_{out}, and the corresponding produced energy E_{out}.
- Net thermal power transferred from the fluid to the block $P_{net} = P_{inj} - P_{out}$, and the cumulative retained energy E_{ret} .
- Thermal loss power to the laboratory P_{loss} and cumulative lost energy E_{loss} .
- Energy stored in the rock E_{rock} .
- Recovered energy during cooling E_{rec} .

2.3.4.1 Fluid-saturated domain

Inside the wells and fractures, heat is transported dominantly by advection. The temperature of the injected water, the temperature of the produced water and the imposed flow rate allow us to determine the thermal power entering P_{inj} and leaving P_{out} the fluid domain at each instant. Their difference gives us the power that is transferred to the block by the fluid P_{net}. When this net power is positive (heating phase), the fluid loses energy to the rock; when it is negative (cooling phase), the fluid extracts energy from the rock.

Integrating these instantaneous powers over the duration of the different phases gives the cumulative injected E_{inj} and extracted E_{out} energies. Their difference represents the energy that has been removed from the fluid during heating $E_{ret}=E_{inj}-E_{out}$, which must have been either stored in the rock or lost to the laboratory. During the pause in-between the heating and cooling phases, the pump is off and no advective heat transport occurs. During this period, $P_{inj}=0$ and $P_{out}=0$ and changes come only from conduction inside the rock and heat losses at its external surfaces.

2.3.4.2 Rock domain

Because we are using non-permeable samples, the rock domain contains no flowing fluid. Heat transport is therefore purely conductive. Two processes occur simultaneously: heat (coming from the fluid) is stored in the rock matrix, and heat escapes to the laboratory through the external surfaces. This loss is one of the main differences between our system and real FTES projects. To estimate this heat loss, we can use the measured surface temperature field of the block. Combined with an effective heat-transfer coefficient h_r (radiative plus convective), they allow us to evaluate how much heat the block releases to the room at each moment. Integrating the loss rate over time then gives the cumulative energy lost to the laboratory.

The energy stored in the rock at any instant E_{rock} is simply the difference between the energy delivered by the fluid E_{ret} and the accumulated heat losses E_{loss}.

2.3.4.3 Identification of the heat-loss coefficient

Some of the long heating phases, in particular those performed on the GABB-11 sample, exhibit a clear thermal plateau. During such periods, the surface temperatures of the block and the outlet temperature evolve only very slowly. In this quasi-steady regime, the rate of change of stored energy in both the fluid and the rock becomes negligible, so that the retained thermal power, denoted P_{ret}, is almost entirely balanced by heat losses to the laboratory. We therefore write $P_{ret}=P_{loss}$.

To model these losses, we use a linear relation of the form:

$$P_{\text{loss}} = h_r\, A_{\text{ext}}\, (\overline{T}_{\text{surf}} - T_0)$$

where A_{ext} is the external surface area of the block and T_{surf} the average surface temperature. Using the plateau of experiment gabb11-25-M, we identify h_r by equating P_{loss} with the value of P_{ret} during the plateau:

$$h_r \approx \frac{\langle P_{\text{ret}} \rangle_{\text{plateau}}}{A_{\text{ext}}\, (\overline{T}_{\text{surf, plateau}} - T_0)}$$

This gives an effective heat-transfer coefficient of $h_r \sim 9.2$ W.m^2/K, which we then use, together with the measured surface temperature curves, to compute the instantaneous loss power P_{loss} and the cumulative lost energy E_{loss} for all experiments.

2.3.4.4 Energy repartition over a complete cycle

In this section we aim to describe how energy is distributed during a full charge–pause–discharge cycle.

During heating, the injected water supplies thermal energy E_{inj}. Part of this energy is immediately carried out at the outlet E_{out}. The rest is retained by the system E_{ret}. This retained energy is then split between heat stored in the rock E_{rock} and heat lost to the laboratory E_{loss} during the heating phase.

During the pause, there is no flow. The block continues to cool by radiation and convection to the room, and therefore the energy stored in the rock decreases.

During cooling, cold water is injected, warms up as it flows through the fractures, and carries energy out of the system. This recovered energy E_{rec} is the useful part of the cycle. At the same time, the block continues to lose heat to the room.

At the end of the experiment, the energy injected E_{inj} during heating has therefore been partitioned into four contributions:
(1) E_{rec}, the energy recovered in the fluid during cooling,
(2) E_{loss}, the energy lost to the laboratory during heating, pause and cooling,
(3) $E_{out,}$ the energy immediately advected out of the block during heating, and
(4) E_{rock} the residual energy still stored in the rock at the end of cooling.

Those contributions are plotted along with their corresponding power in Figure 34.

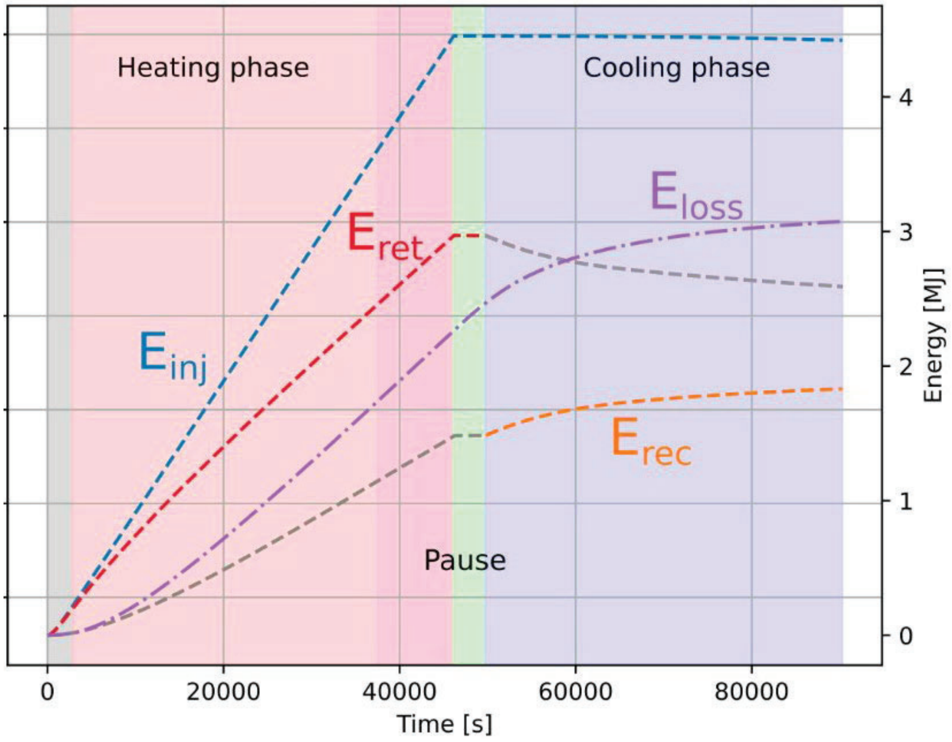

Figure 34. Energy estimation for the heating–cooling cycles of a single FTES experiments performed on the GABB-11 sample with a single fracture open (middle one), injection rate of 25 mL/min and injection temperature of 78 degrees.

2.3.4.5 Thermal Recovery Factor

To assess the performance of a heat-storage cycle in our system, we define a thermal recovery factor (TRF), defined as the fraction of the retained energy that is recovered during the cooling phase:

$$\mathrm{TRF} = \frac{E_{\mathrm{rec}}}{E_{\mathrm{inj}}}$$

This quantity is simply obtained from the inlet and outlet temperature record. In the laboratory system, however, the TRF is strongly affected by external heat losses. Because the block is small and its faces are exposed to ambient air, a large part of the injected energy is lost to the room before it can be recovered. As a result, the measured TRF systematically underestimates the intrinsic thermal performance of the fracture-rock system.

In order to isolate the capacity of the fractured sample itself from the laboratory artefacts, we would like to compute a corrected version of TRF, in which the radiated lost energy is replaced by energy lost through conduction to neighboring rocks. This is exactly the situation we aim to represent in the numerical modelling work done at the lab. In this work, radiative losses at the external faces will be removed and replaced by pure conduction into a larger surrounding rock domain.

Once the individual contributions of injected energy, recovered energy, stored energy and radiative losses are quantified, the relative importance of laboratory artefacts becomes clear. This separation is essential for interpreting the behaviour of the fractured rock volume itself and for comparing the laboratory results with the performance expected from a field-scale system.

This energy budget is shown for a representative experiment (gabb11-25-M) in Figure 35. In this case, the estimated E_{loss} is larger than the “unrecovered” energy (that is, $E_{\mathrm{inj}} - E_{\mathrm{rec}}$). This mismatch indicates that our estimate of the radiative heat-transfer coefficient h_r is likely too high. We also note the very low laboratory TRF (about 8 % for this experiment), which is consistent with the large amount of energy lost to the room by radiation. Similar behavior is observed in the other experiments. The corrected TRF, obtained by replacing radiative losses with conductive storage, provides a more realistic estimate of the performance that would be expected in a field-scale FTES configuration.

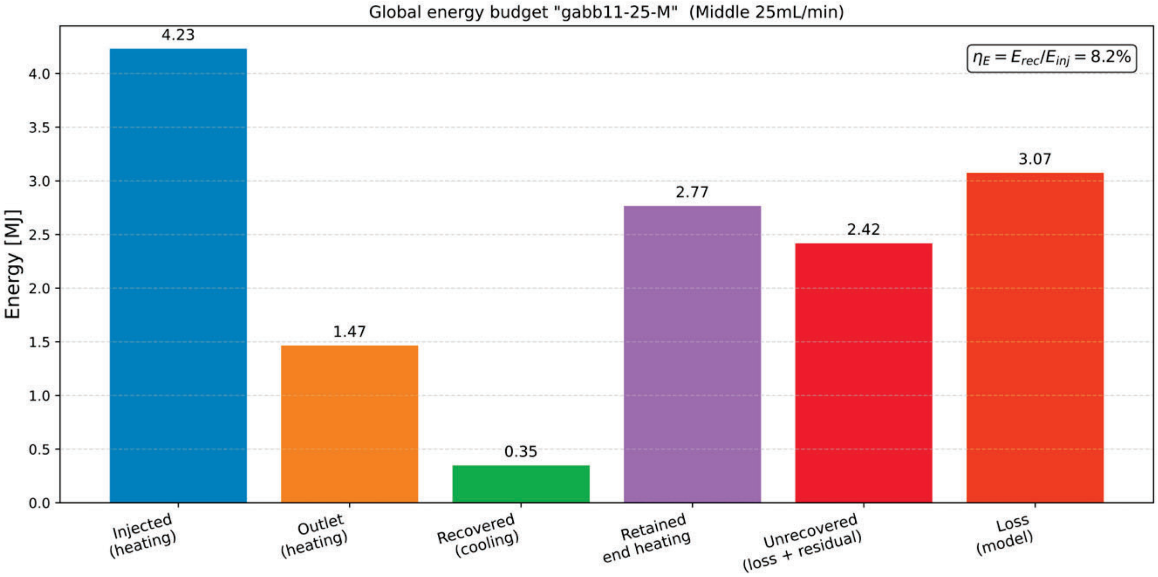

Figure 35. Energy estimation for the heating–cooling cycles of a single FTES experiments performed on the GABB-11 sample with a single fracture open (middle one), injection rate of 25 mL/min and injection temperature of 78 degrees.

2.3.4.6 Effect of repeated cycles

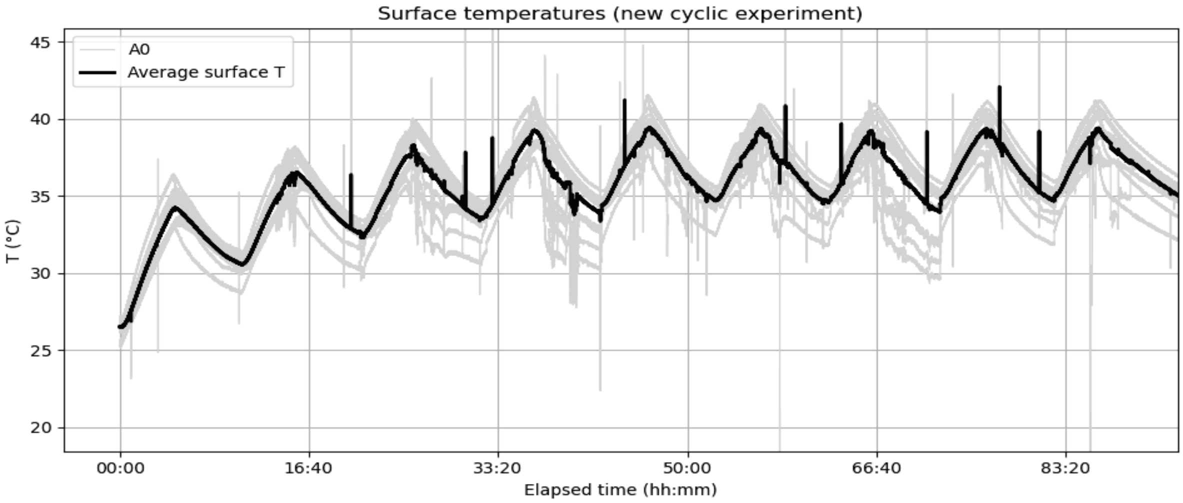

Figure 36. Average surface temperature during the lanh-cycle_9 experiment (Tinj=80 deg, Qinj=5mL/min).

As mentioned earlier, we also studied the evolution of the system for multiple cycles of heating and cooling of the sample. Figure Figure 36 presents the lanh-cycle-9 experiment performed on the LANH-02 sample (single fracture). In this experiment, we injected at 5 mL/min at 80 degrees for 9 consecutive cycles. Over the course of these injections, we observed that the sample did not truly return to its original state in between cycles. Some energy was left in the sample at the end of the first cycle (Figure 36) prompting the second cycle to start with a higher sample temperature. This behavior plateaued after 3-4 cycles to reach an equilibrium. The same trend is observed in the efficiency (defined above) of heat storage (see Figure 37 where over the course of a few cycles a slight increase in system efficiency is observed before it is stabilized and remains constant for following cycles.

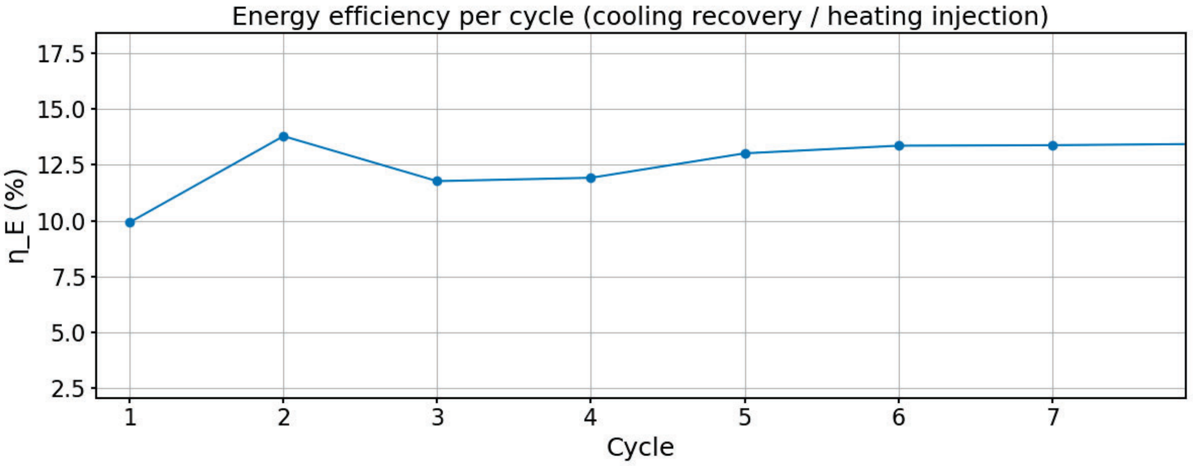

Figure 37. *Efficiency of heat storage for individual cycles of lanh-cycle_9 experiment.*

2.3.5 Conclusion and outlook from laboratory FTES experiments

The laboratory experiments conducted at GEL successfully demonstrate the fundamental physical mechanisms involved in Fracture Thermal Energy Storage, namely injection, storage, and retrieval of thermal energy within fractures in crystalline rock. These tests provide a controlled environment in which flow behavior, fracture connectivity, and thermal response can be examined in detail. However, the measured Thermal Recovery Factor values are not representative of field-scale FTES performance. They are strongly affected by laboratory-specific limitations, including radiative heat losses from the block surfaces and early interaction of the thermal front with the sample boundaries. These effects are not present in real FTES field test and must be considered carefully when interpreting the results.

Fracture transmissibility proved to be a key parameter for FTES operation. As shown by the contrast between the low-transmissibility sample GABB-08 and the high-transmissibility sample GABB-11 in Table 6, insufficient transmissibility can prevent effective injection and circulation. This observation highlights the need to better understand and control transmissibility when designing future FTES systems, both natural and engineered.

The experiments performed on the multiple fracture sample showed that, without flow-control elements, nearly all of the injected fluid flows through the fracture with the highest transmissibility. As a result, the specimen behaved similarly to a single-fracture configuration. Although Inflow Control Devices were included in the completion design, they could not be tested because the sample became blocked by fines. These observations still indicate that some form of flow-control strategy may be necessary to manage fracture-to-fracture variability in field-scale systems. This should be investigated in future work.

During certain experiments performed on low transmissiblity samples (GABB-08 and LANH-02), we observed that injection pressures increased during heating. We interpret this behaviour as thermal expansion of the block causing partial closure of the fracture. Although this response was not consistently reproducible, the observed behavior is similar to the one reported in the decameter-scale tests performed by PNNL (Hibbard et al. 2024). This makes the thermo-mechanical evolution of fractures an interesting direction for future investigation.

The dataset created in this project, including transmissibility estimates, fracture geometries, temperature records and circulation conditions, provides a strong foundation for the development and validation of numerical models. Such models are essential for interpreting laboratory results, bridging the gap between small-scale and field-scale behavior and designing future FTES systems.

2.3.6 Outlook based on laboratory FTES results

The results obtained in this study outline several important directions for future experimental and modelling efforts.

2.3.6.1 Improved boundary conditions and scaling.

The strong influence of heat losses in the current setup shows that better control of boundary conditions is required in order to exactly reproduce a FTES system. Future experiments should explore encasing the specimen in a thermally conductive material such as sand or concrete to approximate subsurface conditions and to limit radiative losses. Numerical models calibrated against the present dataset should guide the design of such improved configurations.

In addition, performing another series of experiments investigating multiple cycles (stopped before reaching steady-state) in the low-power regime are necessary to further strengthen the feasibility of the FTES concept.

2.3.6.2 Investigation of thermo-mechanical evolution.

The pressure increases observed during heating in low-transmissibility experiments, together with similar observations at the decameter scale (Hibbard et al. 2024), indicate that fracture aperture changes during thermal cycling may play an important role. Future experiments could investigate this behavior more systematically and evaluate the long-term evolution of fracture transmissibility and completion integrity.

2.3.6.3 Testing of flow-control strategies.

The transmissibility differences that were observed in our multi-fracture system suggest that flow-control technologies such as ICDs (Inflow Control Devices) may be required to balance flow between fractures. Without them, the low permeability fractures are near invisible to the system. Laboratory testing of ICD performance and alternative solutions under realistic thermal and hydraulic conditions is recommended.

2.3.6.4 Numerical modelling for upscaling and efficiency estimation.

A physic-based numerical model (using for example the DUMUX project (Navarro et al. 2021)) that includes thermal conduction in the rock matrix, advection in fractures and wellbores and heat exchange between water and rock should be developed to study FTES performance in larger, encased volumes. This modelling will help estimate the efficiency of FTES systems under more realistic conditions.

3.0 Work Package 3: Meso-scale FTES demonstration at the Sanford Underground Research Facility

3.1 Design of field-scale test

The scaling analysis described in Section 1.1 were used in combination with the modeling results described in Section 1.2 to develop a testing plan that would achieve as close to full similarity with an envisioned full-scale fracture thermal energy storage system as possible. As part of this a water heater and circulation pump was selected and procured. The water heater was designed to integrate into the existing high-pressure heat exchanger system installed as part of the EGS Collab project.

3.2 Mobilization of equipment to SURF

The water heater was installed and connected to the high-pressure heat exchanger. The straddle packer string from borehole TS had previously been removed from the borehole to allow for geophysical imaging equipment to be deployed. The packer string was reinstalled and tested to facilitate production and injection from all five of the testing boreholes. Although not part of the scope of the DEMo-FTES project, a separate DOE-funded project focusing on geophysical imaging deployed seismic, electrical resistivity, and fiber optic sensing equipment at the testbed during the DEMO-FTES experiments described below. This report does not elaborate on those findings, but the reader is made aware of these data sets that will be valuable for further analysis of the DEMO-FTES data sets.

3.3 Meso-scale field FTES test

Here, we present data, results, and analysis from a decameter-scale field test of fracture thermal energy storage (FTES).

3.3.1 Testbed Description

The Sanford Underground Research Facility (SURF) is an underground research facility in the inactive Homestake Gold Mine (Heise 2015). The facility is in a sequence of metasedimentary, metavolcanic, and intrusive volcanic rocks in the Black Hills of South Dakota (Caddey et al. 1991). The DEMO-FTES project uses an existing test bed in a drift, or horizontal passageway, on the 4100 level (4100 feet or 1,250 meters below the surface) of SURF that was constructed by the EGS Collab project (Figure 38) (Kneafsey et al. 2025). The drift is excavated in the Yates Amphibolite, a massive to faintly banded, moderately well lineated hornblende-plagioclase schist formed from the metamorphosis of an early-Proterozoic basalt (Caddey et al. 1991). On the 4100 level, hornblende and plagioclase dominate the mineralogy, with minor quartz, ankerite, magnetite, ilmenite, epidote, and titanite components (Caddey et al. 1991). Thin (2mm - 2cm) fractures filled with calcite and quartz are common in the formation and a ~10 m thick rhyolite intrusion lies beneath the testbed and intersects the drift away from the testbed (Roggenthen et al. 2024).

The vertical stress on the 4100 level is presumed equal to the lithostatic stress, which is estimated to be approximately 35.4 MPa. The intermediate principal stress is estimated to be between 30 and 40 MPa, and the minimum principal stress, as measured in borehole TV4100 within the testbed, is estimated to be 21.4 MPa, oriented NNE (24-degree azimuth) and plunging approximately 28 degrees. Significant stress heterogeneity was observed around the rhyolite layer in borehole TV4100, where minimum principle stress dropped to 18.6 MPa in the rhyolite layer and 27.6 MPa below the rhyolite layer (Kneafsey et al. 2021; Ingraham et al. 2020).

Extending from the drift into the Yates Amphibolite are five subhorizontal injection/withdrawal boreholes (TU, TS, TL, TC, TN) - used to inject and extract fluids. Four monitoring boreholes (DML, DMU, AML, AMU) are instrumented with a variety of geophysical monitoring equipment. Two characterization boreholes (TV4100 and TH4100) were used for initial site characterization. The injection/withdrawal boreholes form a five-spot well pattern. Each injection/withdrawal borehole can host a straddle packer, two water injection/production lines, two passive pressure sensing lines, and two thermocouples, one of each at the bottom and interval of the packer. The monitoring boreholes are meant to encompass the injection and withdrawal boreholes.

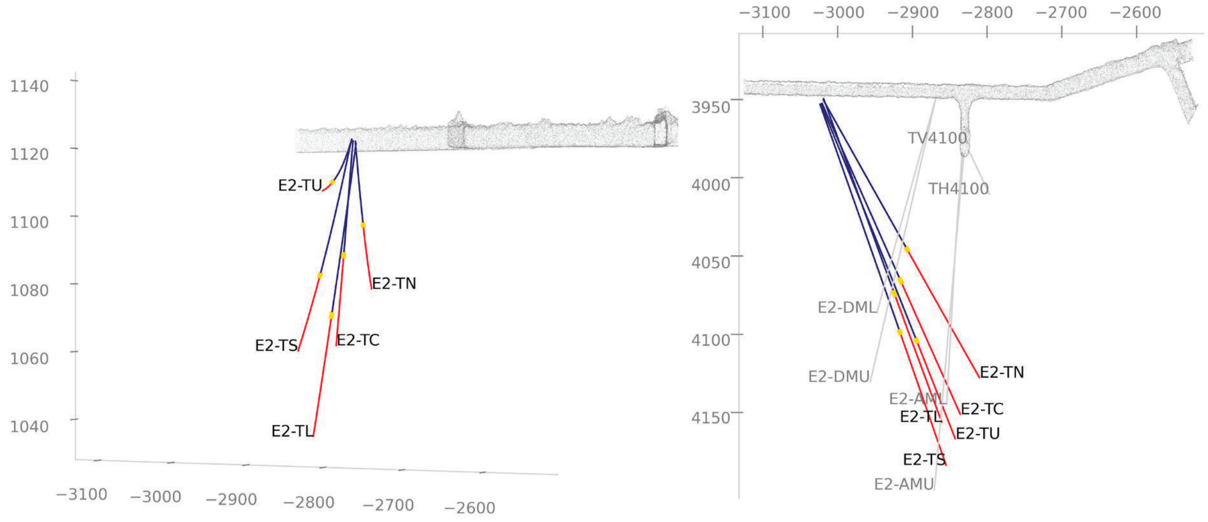

Figure 38. DEMO-FTES test bed from side view (left) and plan view (right). The drift is shown as a grey point cloud. The bottom (red), interval (gold), and collar (blue) sections of the injection and withdrawal boreholes are shown as lines going from the drift into the surrounding rock. The geophysical monitoring boreholes are shown in grey and labelled in black in the right pane. The name of each borehole is labelled in black text at the end of each borehole. Homestake mine coordinates are labelled on the axis in feet.

3.3.2 Test Bed Stimulation

During the EGS Collab project, wells TC and TU were hydraulically stimulated to generate a hydraulic connection between the 5 injection/withdrawal boreholes. At first, the EGS Collab team injected water into zones with existing natural fractures in well TC, below the minimum principal stress, in an attempt to shear and self-prop existing natural fractures (Burghardt et al. 2024). No successful hydraulic connection was made as the shear to normal stress ratio and cohesion of the natural fractures inhibited shear slip.

Then, the EGS Collab team injected water above the minimum principal stress at several depths in wells TC and TU to induce extensional fractures. Three stimulations – at ~195 feet, 170 feet, and 145 feet deep - were performed in well TC (Kneafsey et al. 2025). Injection rates during stimulation varied from a few hundred milliliters per minute to five liters per minute, and the breakdown pressure was around 3,650 psi (25.17 MPa), with some variation between depths. The best hydraulic connection made was with wells TN and TL, which could produce a significant portion (more than 60%) of the injected water at rates exceeding 630 milliliters/minute (Kneafsey et al. 2025). Water was also observed leaking into the drift at around 2840 feet (Figure 1), indicating that the fracture intersected the drift here. A downhole camera revealed that during injection at 145 feet deep in well TC, water was entering the TL borehole from fractures at 154.5 and 160 feet and the TN borehole from a fracture at 148.9 feet. Less water was produced from TS and no hydraulic connection was made with well TU.

One stimulation was performed in well TU to attempt to make a connection between well TU and the rest of the wells. Water was injected into well TU at 178 feet, at one liter per minute and reached a maximum pressure of 5500 psi (37.92 MPa) before reaching a steady state at 4500 psi (31.03 MPa). TC, TN, and TL produced about 25% of the injected volume at this time. During injection into TU, micro seismic events were used to trace fracture growth. The fracture plane approximately had a strike of ~290 and a dip of ~70 degrees, which is consistent with the sections of the boreholes that were producing water and the expression of the fracture intersecting the drift (Kneafsey et al. 2025).

3.3.3 Thermal test

There were two main phases of the field test. The first phase was a “charging” phase. The goal of this phase was to inject hot water into well TC and produce water from the peripheral wells (TN, TS, and TL) to “charge” the fracture network with thermal energy. During this time, the packers in well TC, TL, TN, and TU, were placed at 142.0,170.2,133.6, 177.8 feet down each borehole, respectively. The TS packer was not placed in the borehole because the borehole was hosting temporary geophysical monitoring equipment. Wells TN and TL could produce water from below the packer (bottom), in the packer interval (interval), and above the packer (collar). TS was only able to produce water from the collar because a packer had not been installed in the borehole. TU was shut in, meaning water could not be produced from the interval, to exclude the area of low hydraulic connection around TU from the flow regime. The water injection temperature, rates, and duration, for the FTES test was guided by dimensional analysis of a commercial-scale system (Burghardt et al. 2024), equipment limitations, and logistics.

The second phase was a “discharging” phase. The goal of this phase was to inject ambient temperature water into wells TN and TS which was slightly cooler than the native rock temperature at the site and produce water from well TC, in the hopes that the ambient temperature water would recover the thermal energy injected into the system as it travelled through the fracture network to well TC (Hellström and Larson 2001; Burghardt et al. 2024). During this time, the packers in wells TL, TN, TC, TU, and TS were placed at 149.0,133.6,142.0,177.8 and 166.9 feet down each borehole, respectively. Well TC could produce water from the bottom, interval, or collar. Wells TL and TU were shut in - because we wanted to guide the water flow to well TC where the thermal energy had been stored - but could still produce water from the collar.

Periods of testing and maintenance occurred before the charging phase, between the charging and discharging phase, and after the discharging phase. The goal of the testing and maintenance periods were to establish a hydraulic connection between wells by injecting water and re-opening the fracture network in various wells, and to refine the depths of packers in each borehole to best capture the flow of water through fractures. This testing also allowed us to measure the fracture re-opening pressure (p_{ro}) in several of the boreholes before, in between, and after the charging and discharging phases. We used the fracture re-opening pressure (p_{ro}) as a metric for the compressive stress acting normal to the fracture network at each well (Burghardt et al. 2024; Ito et al. 1999; Whitehead et al. 1989).

Throughout the test, water flow rate - at the bottom, interval, and collar of each well – temperature - at the bottom and interval of each well – and pressure - at the bottom and interval of each well – were recorded at one second resolution.

3.3.3.1 Charging Period December 2024 – February 2025

Water injection into well TC began in December at 2.5 L/min, at ~3800 psi, and ~53 °C (Figure 39). Injection pressure slowly increased to around 5000 psi over the course of injection (Figure 40), requiring the injection rate to be decreased to ~ 2 liters/min at the beginning of January and again to ~1.5 liters/min at the beginning of February to stay within equipment limitations. As a result, the injection temperature decreased to ~48 °C and again to ~ 44 °C because of increased convective heat losses during the waters travel from the heat exchanger to the injection interval (Figure 39).

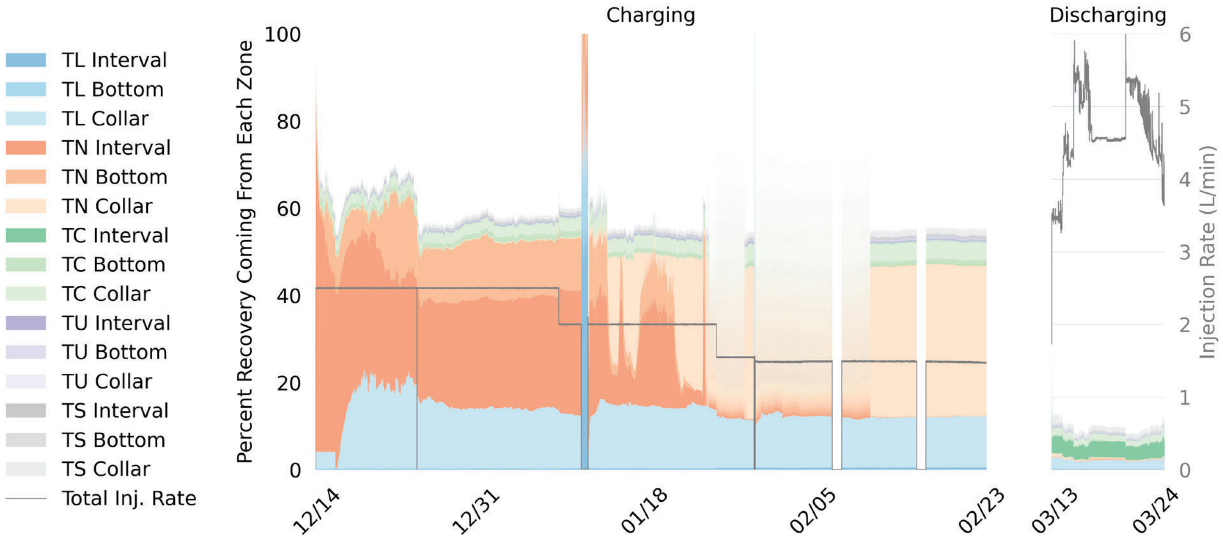

Figure 39. Water injection rate (right y axis, grey line), and water recovery percentage through each production zone of each production well (left y axis) throughout the charging phase (left frame) and discharging phase (right frame).

Between 40 and 60% of the injected water was recovered during this period. Initially, the interval of the TN packer was producing most of this water (~ 55% of the injected water) at rates greater than 1.5 liters/min. Over time water production became more distributed between the interval and bottom of the TN packer and the bottom of the TL packer, where each was producing between ~ 10 and 20% of the injected water at rates between ~300 milliliters/min and 600 milliliters/min. In late January a mechanical issue with the TN packer forced the TN packer to deflate, so all flow coming into well TN was being produced from the collar. Well TC and TS were producing water at low rates (<100 milliliters/min). Water was also observed leaking into the drift where the fracture intersected the drift.

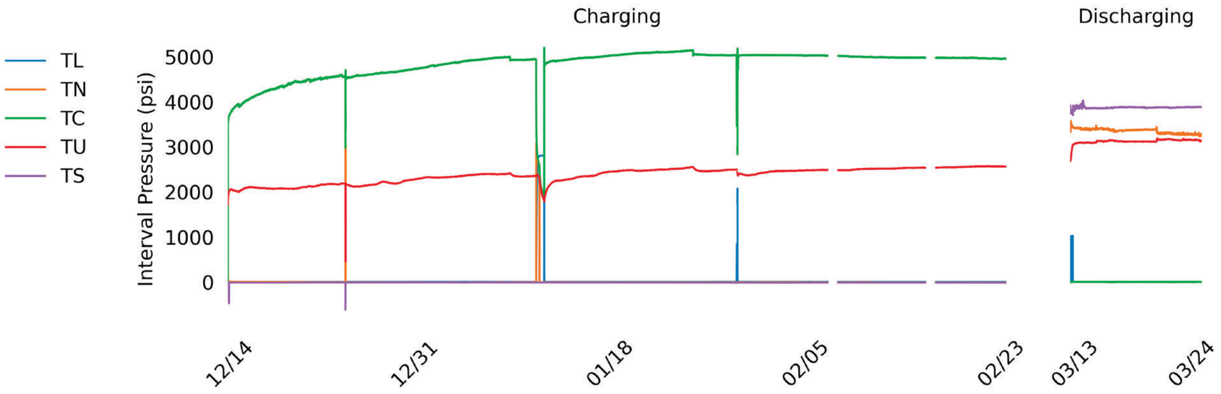

Figure 40. Water pressure measured at each interval in each well throughout the charging phase (left frame) and discharging phase (right frame).

The temperature of the produced water was gradually rising during this period. The ambient temperature of the water in the fracture network was initially around 25 °C. The reader should be alert to the fact that the Joule-Thompson coefficient of liquid water at these temperatures is negative. This means that the temperature rises as the water depressurizes as it moves from the fracture into the production boreholes. This causes the temperature of the produced water to exceed the native rock temperature, and for the magnitude of this difference to depend on the production flow rate. By the end of the charging phase, the water being produced from TN was ~30 °C and the water being produced from TL was ~ 27 °C. This period lasted for about 73 days from December 2024 to the end of February 2025.

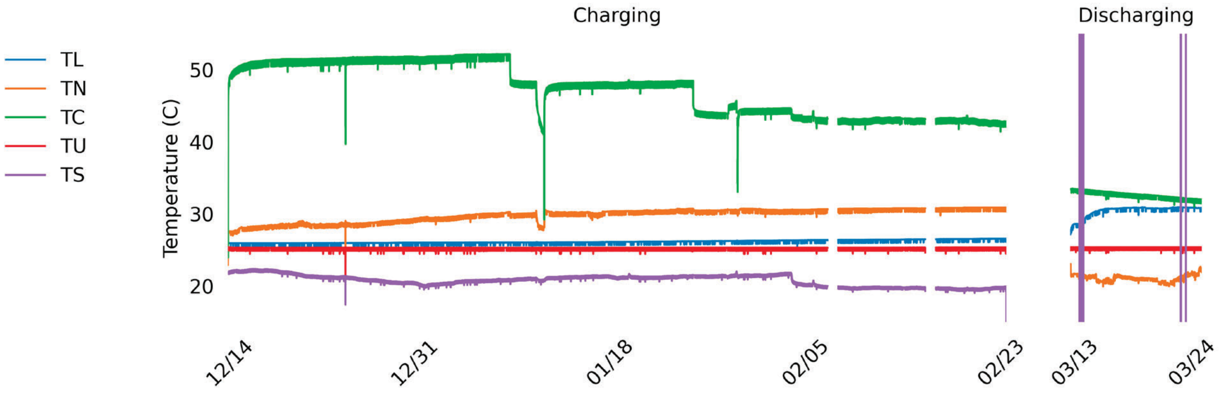

Figure 41. Water temperature measured at each interval in each throughout the charging phase (left frame) and discharging phase (right frame).

3.3.3.2 Discharging Period March 2025

In March, water injection began into TN at up to 3.5 liters/min, ~22 °C, and ~3500 psi, and TS at ~1.5 liters/min, ~22 °C (the ambient temperature of the mine water supply), and ~3900 psi (Figure 41). Injection pressure remained steady for the duration of the discharging phase (Figure 40). Around 10% of the injected water was being recovered during this period. Since the TC interval was the only interval open for production, most of this water was being produced from the TC interval at rates ~200 milliliters/min. Some water (~ <100 milliliters/min each) was also being produced from the collar of well TC, the below the TL packer, and the collar of well TS. Water was also observed leaking into the drift where the fracture intersected the drift. The temperature of the produced water during this period was around 32-34 °C from wells TC and TL (Figure 41). Because of the low water production rates during this period, the test was stopped. This phase lasted for about 10 days total.

3.3.4 Fracture re-opening pressures

Water was injected into three intervals during the testing period in December to re- open the fracture network created during EGS Collab and establish a hydraulic connection between the wells. Water was injected at ~2.5 liters/min into well TU, re-opening the fracture network (p_{ro}) around ~2800 psi and reached a steady-state flowing pressure > 4000 psi. Water was injected at ~2.5 liters/min into well TN, re-opening the fracture network around ~3150 psi and reaching a steady-state flowing pressure (p_f) around 3150 psi. Last, water was injected at ~2.5 liters/min into well TC, re-opening the fracture network around ~3510 psi and reaching a steady-state flowing pressure around 3550 psi (Figure 42) (Table 7).

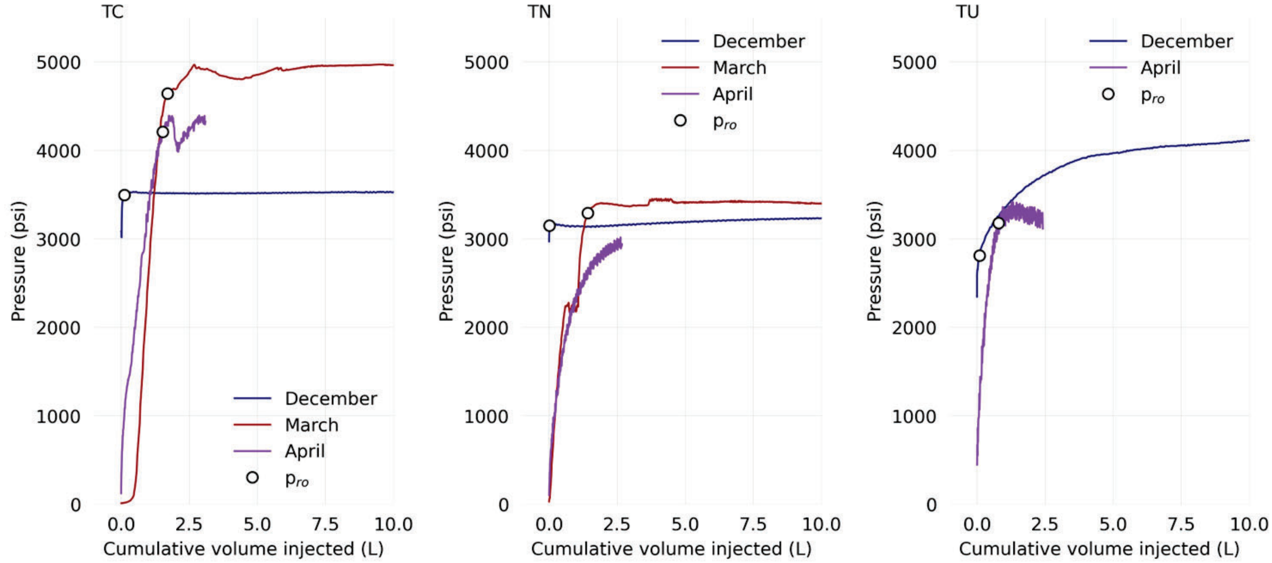

Figure 42. Interval pressure plotted against cumulative water injected for during three testing periods (December, blue line; March, red line; and April, purple line). Data is shown for three wells (TC, left panel; TN, middle panel; and TU, right panel). The fracture re-opening pressure (p_{ro}) is estimated by identifying the pressure at which the slope of the pressure vs cumulative volume injected curve substantially deviates from linearity and is shown as a black circular marker.

In March, water was also injected into three intervals to identify the optimal placement of packers to inject ambient temperature water into the peripheral wells TN and TS and produce water from well TC. Water was injected into well TC at ~1 L/min, re-opening the fracture at ~4650 psi and reaching a steady-state flowing pressure around 4900 psi. Water was injected into well TN at ~1.5 L/min, re-opening the fracture at ~3300 psi and reaching a steady-state flowing pressure around 3400 psi. Finally, water was injected into well TS at ~1.5 L/min, re-opening the fracture at ~4700 psi and reaching a steady-state flowing pressure around 3900 psi.

During the testing period in April, water was injected into four intervals to investigate how the re-opening pressures had evolved after a period of inactivity. The fracture re-opened in borehole TC at~ 4200 psi, TU at ~3200 psi, and TS at ~3800 psi. In well TN, the fracture appeared to take small amounts of water at low pressures, rendering the determination of one fracture reopening pressure difficult. This could be because the fracture at the TN borehole retained a small amount of permeability upon closing (Ito et al. 1999).

Table 7. Estimated fracture re-opening pressures for three wells across three testing periods.

Estimated fracture re-opening pressure (psi)	December	March	April
TC	3510	4650	4200
TN	3150	3300	**
TU	2800		3200
TS		4700	3800

** = low confidence or pressure is leaking into fracture before opening

3.3.5 Discussion of field test results

3.3.5.1 Initial compressive stress heterogeneity on the fracture network

Compressive stress acting normal to the fracture network - as measured by the fracture re-opening pressure (p_{ro}) - varied by up to 700 psi (4.8 MPa) over ~ 15 meters between wells TC, TN, and TU before the thermal test began. One explanation for this observed compressive stress heterogeneity is variations in the orientation and magnitude of stress in the test bed caused by geologic features. For example, natural faults and fractures, the rhyolite dyke observed underneath the test bed, or metamorphic textures and variations in elastic properties (Roggenthen et al. 2024) in the Yates Amphibolite could cause stress heterogeneity in the test bed. All of these features are shown to cause local stress variations in other test beds (Hellström and Larson 2001; Warpinski et al. 1982; Schoenball and Davatzes 2017). Another explanation for this observed compressive stress heterogeneity is a variation in the fracture network orientation relative to the stress field at each borehole. For example, the fracture may have propagated normal to the minimum principal stress in a homogeneous portion of the amphibolite around one borehole, and along a plane of weakness oblique to the minimum principal stress - such as a natural fracture or weak band in the amphibolite - around another borehole (Gischig et al. 2018). In this case, the orientation of the fracture relative to the stress field, and thus the pressure required to re-open the fracture network, would be different in the two boreholes.

3.3.5.2 Induced compressive stress heterogeneity on the fracture network

The compressive stress heterogeneity on the fracture network was exacerbated to more than 1,300 psi (~9 MPa) different between wells TC, TN, and TS during and after the injection of hot water. This was inferred by a substantial increase in the injection pressure (~1,100 psi (7.6 MPa)) required to re-open the fracture network around well TC, where hot water was being injected during the charging phase. The injection pressure required to re-open the fracture network in well TN, where most of the hot water was being produced, was also ~ 150 psi (1.0 MPa) higher after the hot water injection phase then before. One explanation for this increase in compressive stress on the fracture network is an increase in pore fluid pressure (poroelastic effect) and temperature (thermoelastic effect) in the rock matrix surrounding the fracture network (Ghassemi et al. 2008). Many studies have observed thermoelastic effects and poroelastic effects influencing the compressive stress on a fracture network during water injection, although these observations are primarily from geothermal heat extraction, where cool water injection causes a decrease in compressive stress on the fracture network (Guo et al. 2016; Patterson and Driesner 2021, 2020; Ghassemi et al. 2008; Hicks et al. 1996). Because water was flowing into the fracture network at the greatest flowrates and highest temperatures around well TC, the thermoelastic and poroelastic effects would be most pronounced around well TC, which is consistent with what we observe. Around well TN, where water was being produced at lower flowrates and lower but still elevated temperatures, the effects would be present but less pronounced, which is what we observed. After a one-and-a-half-month period of inactivity, the injection pressure required to re-open the fracture network around well TC decreased by around 400 psi (2.7 MPa), likely due to the fracture network around well TC cooling and dispersing pore pressure during the period of inactivity.

3.3.5.3 Effect of stress heterogeneity on hydraulic performance

The low water recovery during the discharging phase of the test relative to the charging phase of the test may be explained by the initial and induced compressive stress heterogeneity on the fracture network. During the charging period, water was being injected into an area with higher compressive stress on the fracture network than the production zone. During the discharging period, water was being injected into an area with lower compressive stress on the fracture network than the production zone. As water preferentially flows to areas of lower compressive stress on fracture networks (Kneafsey et al. 2025; Guo et al. 2016), water injected during the charging phase would preferentially flow towards the production well, whereas water injected during the discharging phase would preferentially flow away from the production well. Further, despite high injection rates in well TN and TS during the discharging period, the injection pressures never exceeded the fracture re-opening pressure measured at well TC before the discharging period. So, water injected into wells TN and TS was prone to travelling elsewhere in the fracture network, escaping the fracture network where it intersects the drift, and possibly extending the fracture network before re-opening the fracture around well TC.

To test this theory, we isolated data from the testing period in December when water was injected into one well and produced from another well to test the hydraulic connection between the two. For each well pair, we used the fracture re-opening pressure (p_{ro}) measured at the injection $p_{ro,inj}$ and production $p_{ro,prod}$ wells to estimate the difference in compressive stress acting normal to the fracture at each well Burghardt et al. 2022; Ito et al. 1999; Whitehead et al. 1989). We then used the distance between the two wells to estimate the compressive stress gradient on the fracture network between the two wells. We compared the compressive stress gradient on the fracture network to the injection impedance (defined as the injection pressure p_{inj} divided by the production flow rate Q_{prod}) between the two wells (Murphy et al. 1999). A higher injection impedance – meaning higher injection pressures are required to recover one unit of water – correlated with a higher positive stress gradient – meaning there is a higher compressive stress acting normal to the fracture around the production well than around the injection well - indicates that the stress gradient between wells controls the hydraulic connection between wells. When injection impedance is plotted against stress gradient, there is a strong, statistically significant positive correlation, supporting the theory that the compressive stress gradient acting normal to the fracture network between any two wells in our test bed controls the hydraulic connection between them (Figure 43).

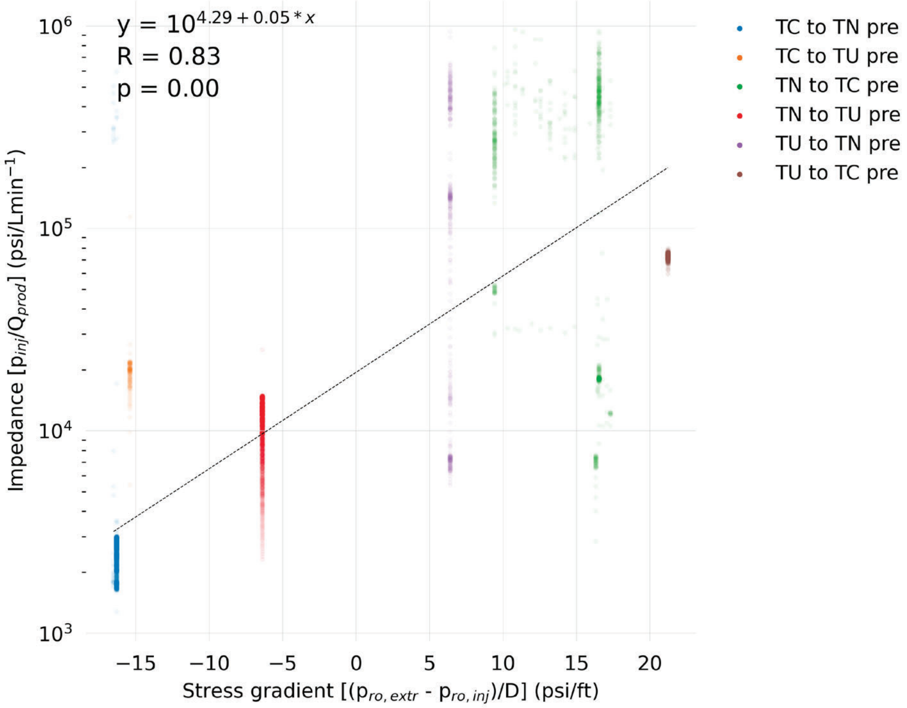

Figure 43. Impedance (injection pressure P_{inj} divided by the production flow rate Q_{prod}) vs compressive stress gradient acting on the fracture network (difference in fracture re-opening pressure at the injection $p_{ro,inj}$ and production $p_{ro,prod}$ wells divided by the distance D between them)r for well pairs tested before hot water injection ("pre"). Each colored dot represents the averaged data from one minute of hydraulic connection between wells. Areas with higher opacity represent a higher concentration of data points. Points are colored according to well pairing.

In field experience and simulations of geothermal energy extraction, a decrease in stress around the cool water injection well is observed (Guo et al. 2016; Patterson and Driesner 2021, 2020; Hicks et al. 1996). During this process, water cools down the area around the injection well more than the area around the production well (Ghassemi et al. 2008). Thus, water is eventually being injected from an area of low relative stress to an area of high relative stress. But these simulations do not observe a dramatic decrease in recovery rate associated with the stress gradient between two wells like we do. This could be because some field experiments of geothermal energy production use proppant to maintains fracture permeability despite high compressive stress on the fracture. Another explanation is that in the geothermal energy extraction scenario, thermal energy is being extracted from the system. So, the induced thermal stresses on the fracture network around the injection well are tensile and do not exceed the fracture extension pressure elsewhere in the test bed. Therefore, when water is injected in the geothermal energy scenario, it is forced to travel from the area of lower relative compressive stress to the more ubiquitous area of higher compressive stress. In the thermal energy storage scenario, the induced thermal stresses on the fracture network around the injection/production well are compressive and can exceed the fracture extension pressure elsewhere in the test bed.

Therefore, water injected into the area of lower compressive stress can travel anywhere in the fracture network, and extend the fracture network, before re-opening the fracture network in the area of higher compressive stress.

Another explanation for the low water recovery rates during the discharging phase of the test could be abiotic or biotic alteration of the fracture network (Viswanathan et al. 2022). A previous test at SURF (Kneafsey et al. 2021) also observed an increase in injection pressure, on the order of 500 psi over 6 months, when injecting cold water into fractured crystalline rock. This effect could not be entirely attributed to poroelastic effects because of the low permeability of the surrounding rock matrix (White et al. 2021).

3.3.6 Implications for future fracture-network technologies

Numerical studies have shown FTES to be thermally and economically effective (Hellström and Larson 2001; Gholizadeh Doonechaly et al. 2024). The gradual increase in production temperature that we observed while injecting hot water indicates that we were “charging” the system with thermal energy. But we were not able to maintain the hydraulic connection necessary between wells to demonstrate the technical feasibility of FTES because of the thermal, hydraulic, and mechanical evolution of the fracture network. There are several options to help overcome this hurdle. One avenue for keeping fractures open, despite increased compressive stress on the fracture, is the use of proppant. Proppants are shown to maintain fracture permeabilities one to two orders of magnitude higher than unpropped fractures at pressures representative of the subsurface (Ahamed et al. 2021). However, the permeability of propped fractures will still decrease with increased compressive stress on the fracture.

3.3.7 Conclusions from field test results

Subsurface fracture networks are increasingly important for geologic resource extraction, resource storage, and waste disposal. The effective and safe use of fracture networks depends on the ability to control and predict their geomechanical, geological, hydraulic, and thermal behavior, which has been tested for a limited number of subsurface technologies and geologic environments. We present preliminary data, results, and analysis from the first decameter-scale test of fracture thermal energy storage in the Sanford Underground Research Facility. The results of this FTES test show that compressive stress heterogeneity on a fracture network can be substantial (~5 MPa) over tens of meters, greatly increase with hot water injection (up to ~9 MPa difference), and is paramount to consider for fluid and energy transfer between wells in fractured rock networks. Injection impedance between injection and production wells shows a strong correlation with the stress gradient between the same wells, suggesting that the hydraulic connection between an injection and production well is directly linked to the difference in compressive stress normal to the fracture around each well. Future work should include testing FTES using proppant, different injection/production configurations.

References

Ahamed, M. A. A., M. S. A. Perera, D. Elsworth, P. G. Ranjith, S. K. M. Matthai, and Li Dong-yin. 2021. “Effective Application of Proppants during the Hydraulic Fracturing of Coal Seam Gas Reservoirs: Implications from Laboratory Testings of Propped and Unpropped Coal Fractures.” *Fuel* 304 (November): 121394. https://doi.org/10.1016/j.fuel.2021.121394.

Burghardt, J., H. A. Knox, T. Doe, et al. 2022. “EGS Stimulation Design with Uncertainty Quantification at the EGS Collab Site.” Paper presented at 56th U.S. Rock Mechanics/Geomechanics Symposium. June 26. https://doi.org/10.56952/ARMA-2022-2224.

Burghardt, J., B. Lecampion, A. Möri, and D. Linneman. 2024. “Design of a Meso-Scale Test of a Fracture Thermal Energy Storage (FTES) System.” Paper presented at 58th U.S. Rock Mechanics/Geomechanics Symposium. June 23. https://doi.org/10.56952/ARMA-2024-0831.

Caddey, Stanton W., Richard L. Bachman, Thomas J. Campbell, Rolland R. Reid, and Robert P. Otto. 1991. *The Homestake Gold Mine, an Early Proterozoic Iron-Formation-Hosted Gold Deposit, Lawrence County, South Dakota*. USGS Report Nos. 1857-J. https://doi.org/10.3133/b1857J.

Detournay, E., and D. I. Garagash. 2003. “The Near-Tip Region of a Fluid-Driven Fracture Propagating in a Permeable Elastic Solid.” *Journal of Fluid Mechanics* 494 (November): 1–32. https://doi.org/10.1017/S0022112003005275.

Feng, Xia-Ting, A. P. Bunger, and B. Lecampion. 2024. “Four Critical Issues for Successful Hydraulic Fracturing Applications.” 1st ed. (London), December 13, 551–93. https://doi.org/10.1201/9781315364223-16.

Finsterle, S., F. Kober, S. Vomvoris, B. Lanyon, and M. B. Kowalsky. 2023. “Data-Worth Analysis for the Design of the HotBENT Monitoring System.” *Geoenergy* 1 (1): geoenergy2023-020. https://doi.org/10.1144/geoenergy2023-020.

Ghassemi, Ahmad, Andrew Nygren, and Alexander Cheng. 2008. “Effects of Heat Extraction on Fracture Aperture: A Poro–Thermoelastic Analysis.” *Geothermics* 37 (5): 525–39. https://doi.org/10.1016/j.geothermics.2008.06.001.

Gholizadeh Doonechaly, Nima, Théo Halter, Alexis Shakas, et al. 2024. “Thermal Energy Storage and Recovery in Fractured Granite Reservoirs: Numerical Modeling and Efficiency Analysis.” *Geosciences* 14 (12): 357. https://doi.org/10.3390/geosciences14120357.

Gischig, Valentin Samuel, Joseph Doetsch, Hansruedi Maurer, et al. 2018. “On the Link between Stress Field and Small-Scale Hydraulic Fracture Growth in Anisotropic Rock Derived from Microseismicity.” *Solid Earth* 9 (1): 39–61. https://doi.org/10.5194/se-9-39-2018.

Guo, Bin, Pengcheng Fu, Yue Hao, Catherine A. Peters, and Charles R. Carrigan. 2016. “Thermal Drawdown-Induced Flow Channeling in a Single Fracture in EGS.” *Geothermics* 61 (May): 46–62. https://doi.org/10.1016/j.geothermics.2016.01.004.

Heise, J. 2015. “The Sanford Underground Research Facility at Homestake.” *Journal of Physics: Conference Series* 606 (1): 012015. https://doi.org/10.1088/1742-6596/606/1/012015.

Hellström, Göran, and Sven Larson. 2001. “Seasonal Thermal Energy Storage – the HYDROCK Concept.” *Bulletin of Engineering Geology and the Environment* 60 (2): 145–56. https://doi.org/10.1007/s100640100101.

Hibbard, Leon, Jeffrey A. Burghardt, Dana Sirota, Yingqi Zhang, Brice T. Lecampion, and Dorothy Linneman. 2024. “Design and Operation of a Meso-Scale Fracture Thermal Energy Storage Test.” *AGU Fall Meeting Abstracts* 2024 (1075): H23G-1075. https://ui.adsabs.harvard.edu/abs/2024AGUFMH23G.1075H/abstract.

Hicks, T. W., R. J. Pine, J. Willis-Richards, S. Xu, A. J. Jupe, and N. E. V. Rodrigues. 1996. “A Hydro-Thermo-Mechanical Numerical Model for HDR Geothermal Reservoir Evaluation.” *International Journal of Rock Mechanics and Mining Sciences & Geomechanics Abstracts* 33 (5): 499–511. https://doi.org/10.1016/0148-9062(96)00002-2.

Ingraham, M. D., P. C. Schwering, J. Burghardt, et al. 2020. “Analysis of Hydraulic Fracturing on the 4100 Level at the Sanford Underground Research Facility.” Paper presented at 54th U.S. Rock Mechanics/Geomechanics Symposium. June 28. https://dx.doi.org/.

Ito, T., K. Evans, K. Kawai, and K. Hayashi. 1999. “Hydraulic Fracture Reopening Pressure and the Estimation of Maximum Horizontal Stress.” *International Journal of Rock Mechanics and Mining Sciences* 36 (6): 811–26. https://doi.org/10.1016/S0148-9062(99)00053-4.

Kneafsey, Tim, Doug Blankenship, Pat Dobson, Mark White, and Joseph P. Morris. 2021. “Fracture Stimulation and Chilled-Water Circulation Through Deep Crystalline Rock: Characterization, Modeling, Monitoring, and Heat-Transfer Assessment.” Paper presented at Stanford Geothermal Workshop. *PROCEEDINGS, 46th Workshop on Geothermal Reservoir Engineering*.

Kneafsey, Tim, Pat Dobson, Doug Blankenship, et al. 2025. “The EGS Collab Project: Outcomes and Lessons Learned from Hydraulic Fracture Stimulations in Crystalline Rock at 1.25 and 1.5 Km Depth.” *Geothermics* 126 (February): 103178. https://doi.org/10.1016/j.geothermics.2024.103178.

Lecampion, Brice, and Jean Desroches. 2015. “Simultaneous Initiation and Growth of Multiple Radial Hydraulic Fractures from a Horizontal Wellbore.” *Journal of the Mechanics and Physics of Solids* 82 (September): 235–58. https://doi.org/10.1016/j.jmps.2015.05.010.

Liu, Dong, and Brice Lecampion. 2022. “Laboratory Investigation of Hydraulic Fracture Growth in Zimbabwe Gabbro.” *Journal of Geophysical Research: Solid Earth* 127 (11): e2022JB025678. https://doi.org/10.1029/2022JB025678.

Murphy, Hugh, Donald Brown, Reinhard Jung, Isao Matsunaga, and Roger Parker. 1999. “Hydraulics and Well Testing of Engineered Geothermal Reservoirs.” *Geothermics* 28 (4): 491–506. https://doi.org/10.1016/S0375-6505(99)00025-5.

Navarro, M., T. Kock, and P. Bastian. 2021. “DuMuX-an Open-Source Simulator for Solving Flow and Transport Problems in Porous Media.” *Computers & Mathematics with Applications*. https://kuleuven.limo.libis.be/discovery/fulldisplay/lirias3438290/32KUL_KUL:Lirias.

Patterson, James W., and Thomas Driesner. 2020. "The Effect of Thermo-Elastic Stress Re-Distribution on Geothermal Production from a Vertical Fracture Zone." *Geothermics* 85 (May): 101745. https://doi.org/10.1016/j.geothermics.2019.101745.

Patterson, James W., and Thomas Driesner. 2021. "Elastic and Thermoelastic Effects on Thermal Water Convection in Fracture Zones." *Journal of Geophysical Research: Solid Earth* 126 (2): e2020JB020940. https://doi.org/10.1029/2020JB020940.

Ramstad, R. K., B. O. Hilmo, B. Brattli, and H. Skarphagen. 2007. "Ground Source Energy in Crystalline Bedrock-Increased Energy Extraction Using Hydraulic Fracturing in Boreholes." *Bulletin of Engineering Geology and the Environment* 66 (4): 493–503. https://doi.org/10.1007/s10064-007-0100-7.

Roggenthen, W., Timothy Kneafsey, J. Burghardt, et al. 2024. *Complementary Subsurface Characterization Methods to Develop a Geologic Model for the EGS Collab Experiment, Sanford Underground Research Facility*. https://escholarship.org/uc/item/9bn6j5xz.

Schoenball, Martin, and Nicholas C. Davatzes. 2017. "Quantifying the Heterogeneity of the Tectonic Stress Field Using Borehole Data." *Journal of Geophysical Research: Solid Earth* 122 (8): 6737–56. https://doi.org/10.1002/2017JB014370.

Viswanathan, H. S., J. Ajo-Franklin, J. T. Birkholzer, et al. 2022. "From Fluid Flow to Coupled Processes in Fractured Rock: Recent Advances and New Frontiers." *Reviews of Geophysics* 60 (1): e2021RG000744. https://doi.org/10.1029/2021RG000744.

Warpinski, Norman R., Richard A. Schmidt, and David A. Northrop. 1982. "In-Situ Stresses: The Predominant Influence on Hydraulic Fracture Containment." *Journal of Petroleum Technology* 34 (03): 653–64. https://doi.org/10.2118/8932-PA.

White, M. D., J. A. Burghardt, and EGS Collab Team. 2021. "Modeling the Dynamic Flow Resistance Across the Fracture Network of EGS Collab Experiment 1." Paper presented at Stanford Geothermal Workshop. *PROCEEDINGS, 46th Workshop on Geothermal Reservoir Engineering*.

Whitehead, W. S., J. M. Gatens, and S. A. Holditch. 1989. "Determination of *in Situ* Stress Profiles through Hydraulic Fracturing Measurements in Two Distinct Geologic Areas." *International Journal of Rock Mechanics and Mining Sciences & Geomechanics Abstracts* 26 (6): 637–45. https://doi.org/10.1016/0148-9062(89)91444-7.

Zhang, Yingqi, Lehua Pan, Karsten Pruess, and Stefan Finsterle. 2011. "A Time-Convolution Approach for Modeling Heat Exchange between a Wellbore and Surrounding Formation." *Geothermics* 40 (4): 261–66. https://doi.org/10.1016/j.geothermics.2011.08.003.

Pacific Northwest
National Laboratory

902 Battelle Boulevard
P.O. Box 999
Richland, WA 99354
1-888-375-PNNL (7665)

www.pnnl.gov